Order Number 1342954

Novel Fourier methods for biomagnetic boundary value problems

Cameron, Seth Andrew, M.S.

The University of Arizona, 1990

U·M·I
300 N. Zeeb Rd.
Ann Arbor, MI 48106

NOVEL FOURIER METHODS FOR BIOMAGNETIC BOUNDARY VALUE PROBLEMS

by
Seth Andrew Cameron

A Thesis Submitted to the Faculty of the
COMMITTEE ON OPTICAL SCIENCES (GRADUATE)
In Partial Fulfillment of the Requirements
For the Degree of
MASTER OF SCIENCE
In the Graduate College
THE UNIVERSITY OF ARIZONA

1990

STATEMENT BY AUTHOR

This thesis has been submitted in partial fulfillment of requirements for an advanced degree at The University of Arizona and is deposited in the University Library to be made available to borrowers under rules of the Library.

Brief quotations from this thesis are allowable without special permission, provided that accurate acknowledgment of source is made. Requests for permission for extended quotation from or reproduction of this manuscript in whole or in part may be granted by the head of the major department or the Dean of the Graduate College when in his or her judgement the proposed use of the material is in the interests of scholarship. In all other instances, however, permission must be obtained from the author.

SIGNED: Seth A. Cameron

APPROVAL BY THESIS DIRECTOR

This thesis has been approved on the date shown below:

William J. Dallas — December 13, 1990

William J. Dallas
Professor of Optical Sciences

Date

Table of Contents

List of Figures 4

Introduction

Chapter 1

Electrophysiology and Biomagnetic Imaging 9

A Phantom Test-bed 11

Theory

Chapter 2

Fourier Projection Theory 16

Applications

Chapter 3

The Volume Current Problem 27

The Volume Current Algorithm 29

Direct calculation for a dipole in a half-space 35

Direct calculation for a dipole in a sphere 39

Chapter 4

Magnetic Field Extrapolation 47

Internal Magnetic Field Reconstruction 53

Summary and Conclusion 57

Appendices

Appendix A

Fourier Biot-Savart and transform of $\mathbf{r}/r^3$ 58

Appendix B

Direct calculation for half-space conductivity 59

List of Figures

Figure	Page
1.1 - Current dipole model for axon depolarization	10
1.2 - Current dipole phantom source	13
1.3 - Schematic of the magnetic field mapping system	14
2.1 - A delta function in real space	20
2.2 - Delta function Fourier transform	21
2.3 - Radial projection of delta function Fourier transform	21
2.4 - Electric dipole moment	22
2.5 - Electric dipole return field	23
2.6 - Tangential projection of delta function Fourier transform	24
2.7 - Current dipole moment	25
2.8 - Current dipole return field	26
3.1 - Impressed current source	30
3.2 - Fourier tangential operation on impressed source	30
3.3 - Result of current confinement operation	31
3.4 - Electric field generated by current source plus conductivity gradients	31
3.5 - Fourier radial correction of electric field	33
3.6 - New prediction for total current density	33
3.7 - A vertical dipole in a half-space of homogeneous conductivity	35
3.8 - Predicted electric field from 3.7	36
3.9 - Predicted current field from 3.7	37
3.10 - Predicted surface current from 3.7	37
3.11 - Predicted magnetic field from 3.7	38

3.12 - A vertical dipole in a sphere of uniform conductivity 39

3.13 - A vertical dipole in an infinite space of uniform conductivity 40

3.14 - Analytic and predicted magnetic fields of 3.12 and 3.13 41

3.15 - Analytic and predicted magnetic fields of 3.12 and 3.13 42

3.16 - Analytic and predicted magnetic fields of 3.12 and 3.13 43

3.17 - Smooth reconstruction of dipole field using Fourier radial operation 45

3.18 - Poor reconstruction of dipole field using Fourier radial operation 46

4.1 - A current loop phantom source 49

4.2 - Surface magnetic data from 4.1 50

4.3 - External extrapolation of 4.2 51

4.4 - Analytic and predicted external magnetic field from 3.10 52

4.5 - An internal solution to the magnetic field in 4.3 54

4.6 - Surface current solution for current loop 4.1 55

4.7 - Top surface current solution for current loop 4.1 55

4.8 - An internal reconstruction of the magnetic field from 4.4 A) 56

4.9 - Surface currents that generate 4.8 56

Abstract

A novel Fourier technique for solving a wide variety of boundary value problems is introduced. The technique, called Fourier projection, is based on the geometric properties of vector calculus operators in reciprocal space. Fourier projection decomposes arbitrary vector fields into collections of irrotational and/or divergenceless dipole subfields. For well-posed problems, Fourier projection algorithms can calculate unknown field values from a knowledge of primary sources and boundary conditions. Specifically, this technique is applied to several problems associated with biomagnetic imaging, including volume current calculations and equivalent surface current solutions. In addition, a low-cost magnetic field mapping system designed to aid reconstruction algorithm development is described.

Chapter 1

Introduction

Real-time imaging of activity within the brain is an intriguing goal. Most brain activity involves the transfer of information in the form of small currents that travel along the lengths of neurons. Tracing these currents, like tracing a telephone call, maps communication within the system. Although we may not know what is said, in our effort to understand the nervous system, just knowing which cells are talking can be very informative.

Most nervous systems are at once extraordinarily complex and difficult to observe in their functioning environment. Invasive microelectrodes provide some information but are usually damaging and therefore rarely used to study the intricate human nervous system. Instead, researchers and physicians historically have attempted to observe the human nervous system through careful measurement of surface electric potentials. A well known example is the electroencephalogram (EEG) which records relative changes in the electric potential over the scalp. Unfortunately, after years of analysis, the electrogenesis of surface potential waveforms is still not fully understood. Although these mappings have established some clinical usefulness, they cannot provide the detailed information necessary to localize neural activity generated within specific regions of the brain. The technique's sensitivity to electrical conductivity variations within and between tissues contributes to source localization difficulties. Because the electric potential generated at source locations is altered significantly by electrical conductivity variations in the tissue between the source and the measurement locations, reconstructing internal potentials from surface potential maps is extremely difficult. The search for a better technique continues.

With the advent of the superconducting quantum interference device (SQUID) in the late 1960's, it became possible to detect and record the magnetic fields generated by neuronally activated currents. Because most tissue has a permeability nearly equal to that of free space, magnetic field generated at source locations is not significantly altered by tissue between the source and the external measurement. This sparked hope that biologically generated magnetic fields could provide the information not available with the

EEG. In 1972, Plonsey[1] demonstrated that biomagnetic field measurements did indeed promise new information. Specifically, he showed that the curl of source currents produces magnetic fields whereas their divergence produces surface potentials. The curl and divergence can be independent, and thus, the magnetic field can provide alternate information.

Biomagnetic imaging strives to produce three-dimensional reconstructions of current paths based on measurements of the external magnetic field produced by those currents. Unfortunately, this inverse problem is not unique. There exist many internal current configurations that generate the same external field. For example, one possible reconstruction can always be formulated by currents allowed to flow only at the surface of a given volume conductor. Since such an answer has no physiological basis, reconstruction algorithms should be designed to suppress this errant solution. In other words, researchers hope to restrict the possible solution set by applying *a priori* knowledge. However, exactly what types of current paths to expect is uncertain. The current fields produced by neurons isolated *in vitro* have been accurately modeled, but thousands of neurons operating in conjunction could produce a rather different form. Still, the information to be gained from even a partially functioning imaging system is worth spending effort to achieve. Indeed, the most basic biomagnetic model, a single dipole within a homogeneous spherical head, has proved clinically useful for the surgical treatment of focal epilepsy[2].

This paper presents a novel method for solving boundary value problems using Fourier analysis. Its emphasis will address problems specific to biomagnetic imaging, but the techniques should prove equally applicable to problems encountered in other disciplines, ranging from thermal physics to fluid dynamics. The remainder of this chapter will describe some physiology and terminology associated with biomagnetic imaging and present an experimental test facility established to help verify the effectiveness of the algorithms. Chapter 2 develops the theory behind Fourier projection operation which is then applied in Chapters 3 and 4. Chapter 3 presents a numeric algorithm to solve the

---

[1]Plonsey, R.W. 1972, Comparative capabilities of electrocardiography and magnetocardiography, Am. J. of Cardiol. 29:735-736.

[2]Schneider, Siegfried et al. Multichannel Biomagnetic System for Study of Electrical Activity in the Brain and Heart. Radiology, 1990 Vol 176, No. 3, 825-830.

volume current problem, while Chapter 4 concentrates on issues regarding magnetic field extrapolation and equivalent surface current solutions.

Electrophysiology

Most bioelectric current is generated as a result of ion exchange during neural signal transmission[1]. The axon of a neuron is the narrow channel used to convey signal from one neuron to the next. It has a specialized membrane that separates interior cytoplasm from extracellular fluid and regulates the relative concentration of ions within those fluids. The membrane is quite permeable to K+ ions but may change its permeability to Na+ ions depending upon its state of activity. Due to large negatively charged organic ions fixed within the axon, the interior has a slightly negative potential. To achieve a state of equilibrium, K+ ions flow into the cell until the the electric potential pulling them in is balanced by the concentration gradient pushing them out. Thus, the K+ ions cannot completely neutralize the cell which maintains a slightly negative internal resting potential of approximately -70 mV.

The key to operation lies in an active transport of interior Na+ ions across the cell membrane. Normally, this establishes a relative paucity of Na+ inside the cell. As a polarizing signal arrives, the membrane suddenly becomes much more permeable to Na+ ions which flood inside. During this polarization phase, the excess Na+ ions reverse the potential to approximately 50mV. To repolarize and prepare for another signal, K+ ions rush out, descending the potential and concentration gradient, and the cell resumes active expulsion of Na+ ions. However, before expulsion, some of the Na+ influx spreads down the axon interior and initiates further depolarization. This spreading serves to propagate the signal at rates up to 25 m/sec.

---

[1]Churchland, P.S. Neurophilosophy: Toward a Unified Science of the Mind/Brain. p.48, MIT Press, Cambridge 1986.

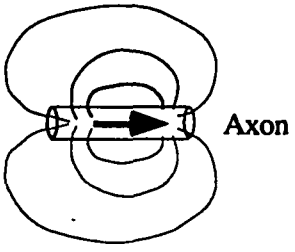

Figure 1.1: Current dipole model for neuronally generated ion flow

A series of alternating current dipoles is the most common model used to describe ion motion established during axon transmission. Because the ion motion persists for a sufficient time (i.e. a quasi-static state is established), the static form of the Maxwell equations is used to describe the physics. This means that the electric current is allowed no divergence, and the electric field is allowed no curl,

$$\nabla \cdot \mathbf{J} = 0 \quad \text{and} \quad \nabla \times \mathbf{E} = 0.$$

The current dipole field is similar to that produced by a tiny battery placed into a conducting solution. In an isotropic medium of infinite extent, the current paths external to the dipole source are determined by the electric field established at the terminals. Because static electric fields must have zero curl, the current within the dipole needs another mechanism of transport to flow against the electric field between the poles. A battery, for example, maintains a large chemical potential at its terminals to transport charge against its internal electrical potential gradient.

In biomagnetism, the internal current of a dipole is referred to as the impressed current source, while the external ohmic currents are called volume currents. This distinction is emphasized to improve clinical applicability. A brain surgeon, for instance, is interested in locating accurately the source of an epileptic disturbance. Knowledge of volume current paths for such applications is superfluous if not undesirable. However, volume currents play a significant role in the production of magnetic fields. If one hopes to reconstruct internal magnetic fields accurately, it is doubtful that volume current effects may simply be ignored.

A classic example of volume current contribution occurs for a current dipole placed vertically in a half-space of homogeneous conductivity. Above the half-space plane, the conductivity is zero so that the volume currents must be confined to the volume beneath the plane. Surprisingly, this configuration generates no magnetic field above the plane! The volume current contribution to the external magnetic field is equal and opposite to the impressed current contribution. Such "magnetically silent" sources also exist for spherical conducting media. In a spherically symmetric environment, dipoles directed along radii create no external magnetic field. Consequently, using spherical symmetry to model the human head immediately removes any possibility of reconstructing radially oriented dipole components of a current distribution.

By contrast, horizontal dipoles beneath a plane or tangentially oriented dipoles in a sphere produce relatively undistorted external magnetic fields. For this reason, the most common "solution" to the biomagnetic inverse problem is found by fitting a single equivalent current dipole oriented tangentially in a spherical head. This technique has demonstrated substantial utility for locating epileptic foci but is unsatisfactory for general clinical and research applications. For instance, if two centers of activity fire, this model will likely provide misleading information by locating a single dipole somewhere between the actual sources. If greater reconstruction reliability can be achieved, magnetoencephalography (MEG) will become an important research and diagnostic tool.

Because biomagnetic imaging is a non-invasive technique, verifying reconstructions is challenging. For *in vivo* measurements, the current sources are unknown, so one has no means to judge the accuracy of a reconstruction. The alternative is to measure phantoms for which the current sources are controlled. For this purpose, a magnetic test-bed was created.

Experimental Test-bed

Verifying performance on real and/or analytic data is a crucial aspect of algorithm development. Without testing, simulation performance can be quite misleading. For instance, certain internal reconstruction Fourier techniques provide remarkable results when applied to numerically generated fields. Information apparently becomes encoded in high-frequency components not properly removed when one deletes internal field values. Upon

reconstruction, the high frequencies replace noticeable traces of the original field back into the interior. Regrettably, such hidden information is not present in actual data. The same algorithm fails to reconstruct internal sources using untainted data.

Due to the expense and sophistication of SQUID based technology, only a few centers around the world are able to record biologically generated signals which lie in the picoTesla range. Nevertheless, there are certain advantages for studying the magnetic reconstruction problem apart from its biological origins. Most notably, one has control over the form and location of current sources. Unlike *in vivo* experiments, phantom reconstructions may be compared with known source locations.

For this work, a phantom test-bed was established based on a tri-axial fluxgate magnetometer. The magnetometer was sensitive to about 1 microgauss ($1x10^{-10}$ Tesla), but its sensitivity could not be fully utilized do to a lack of magnetic shielding. The common building environment is replete with background magnetic induction. There is a large (0.5 gauss) but reasonably stable contribution from the earth's magnetic field and smaller (0.005 gauss) quite unstable 60Hz signals due to power distribution lines within the building. To acquire data in this hostile environment, the following noise filtering scheme was implemented.

First, the detector was mounted such that it remained fixed with respect to the earth's magnetic field. With its d.c. offset, the magnetometer could null a static field up to 1.2 gauss. Next, the analog signal from each channel was directed through its own low-pass active filter set to cut-off frequencies above approximately three Hertz. Lastly, a microcomputer with a multichannel analog to digital board was used to collect and average multiple samples for each field measurement.

Despite heavy filtering, further care had to be exercised while taking data. For example, motion of metal chairs located in an adjacent room was enough to cause problems. Displacement of objects with high magnetic susceptibility would warp the earth's field such that the precision d.c. offset was no longer correct. To abate these sources of error, the computer was programmed to pulse current through the sources. First, a background measurement (the average of ten samples) was recorded. Then, the current sources were activated, and another measurement recorded. The difference between the background and source averages was registered as the source field strength at

that location. Finally, the volume containing the phantom source was translated by hand against a stationary grid to record subsequent background and source values.

Two forms of sources were designed: a current loop and a current dipole. The loop consisted of seven turns of wire around a plastic tube. Current was fed to the loop via a twisted pair to minimize extraneous magnetic field contribution. About one ampere of current would yield reproducible results, essentially swamping residual noise with signal.

The current dipole proved more challenging to produce. Typically, researchers submerge a dipolar probe into a saline solution as a means to model the current dipole. However, this noisy environment required current densities much greater than electrolytic solutions conduct gracefully. Corrosion and electrolysis forced a new approach. Instead, a metal alloy of low melting temperature and low magnetic susceptibility was used as the volume conductor. A coaxial cable with its center conductor extended served as the dipolar electrode. The cable was imbedded into a molten volume of Wood's metal (mostly lead, bismuth, and tin) that was subsequently allowed to solidify. This construction made electrons the current medium in contrast to the ions of an electrolytic solution. Because the dipole current source produced a weaker magnetic field than the current loop, and because the dipole could not scale with multiple turns, as much as 20 amperes were necessary to yield reproducible results. The duty cycle of each current source was regulated by a computer controlled solenoid switch. The pulses were about 4 seconds in duration to provide enough relaxation time for the active filtering. Below are schematics of a dipole source and the phantom test bed.

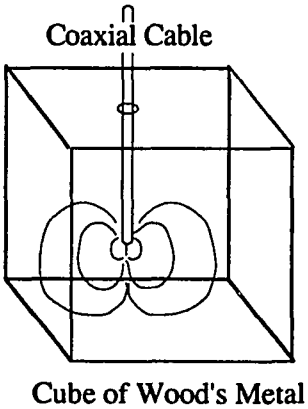

Figure 1.2: Current dipole phantom source

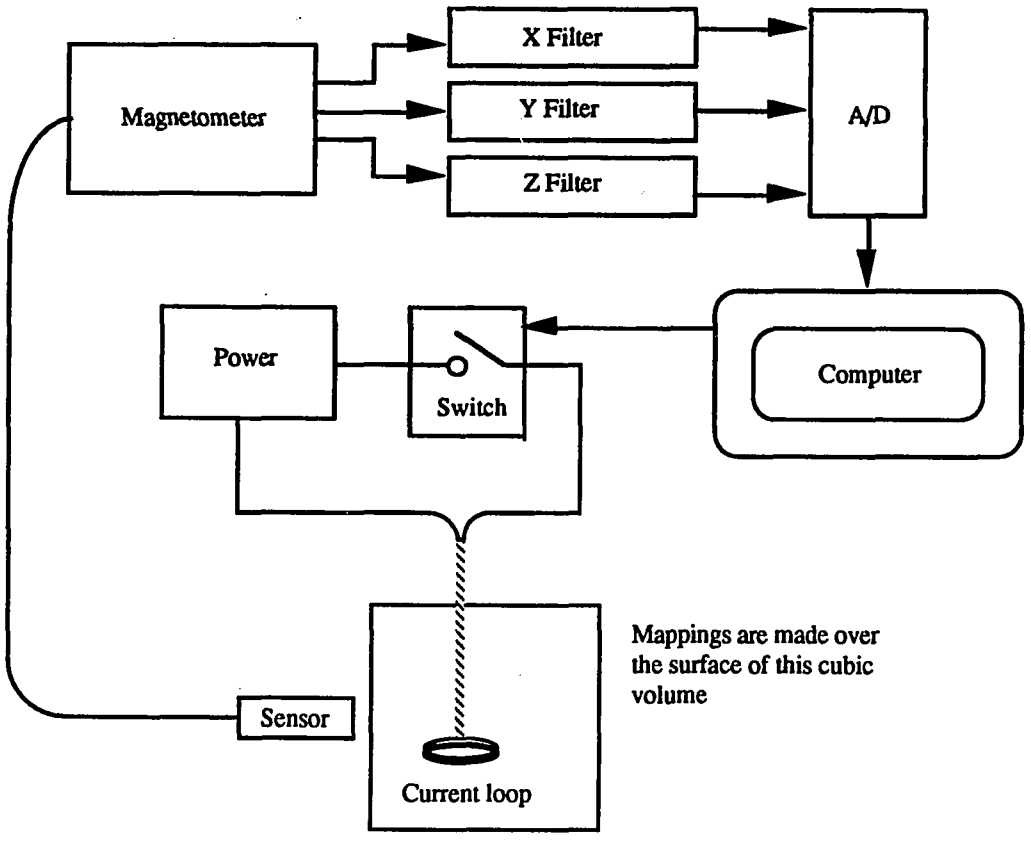

Figure 1.3: Schematic of the magnetic field mapping system

The test-bed is a proof-of-principle design which demonstrates a means to conduct magnetic imaging research without top quality SQUID technology and magnetic shielding. The system allows significant control over the types of sources, geometries, and conductivities involved. Because the nonuniqueness of magnetic reconstruction solicits the introduction of *a priori* information involving conductivity and source structure, this type of test-bed should be valuable for future algorithm development. Results from actual measurements using this testbed will be presented in chapter 4.

Chapter 2

Fourier Projection Theory

Fourier transformation provides a means of describing mathematical functions in frequency space. Explicitly, the transform and its inverse are

$$\tilde{F}(\rho) = \iiint_{r=-\infty}^{\infty} f(\mathbf{r}) e^{-i2\pi(\mathbf{r}\cdot\rho)} d\mathbf{r} \quad \text{and} \quad f(\mathbf{r}) = \iiint_{\rho=-\infty}^{\infty} \tilde{F}(\rho) e^{i2\pi(\mathbf{r}\cdot\rho)} d\rho.$$

These integrals transform cartesian real space coordinates, $\mathbf{r} = (x,y,z)$ into Fourier space coordinates, $\rho = (\xi,\eta,\zeta)$ and vice versa. Although Fourier transformation is also defined for other coordinate systems, Cartesian coordinates provide a certain simplification since vector fields may be transformed by applying the above integrals to each component separately.

A remarkable consequence of Fourier transformation is that the real space derivative operation becomes simple spatial frequency multiplication in the Fourier domain,

$$\iiint_{r=-\infty}^{\infty} \nabla f(\mathbf{r})\, e^{-i2\pi(\mathbf{r}\cdot\rho)} d\mathbf{r} = i2\pi\rho\tilde{F}(\rho).$$

Similarly, real-space vector calculus operations become vector algebraic operations in frequency space.

Biomagnetic processes evolve slowly enough to be described by the static form of the Maxwell and continuity equations. If these equations are transformed to the Fourier domain, several important features of static magnetic, current, and electric fields emerge. Below are the relevant Maxwell and continuity equations with their accompanying Fourier transforms. For simplicity, the constants which determine the relative strengths of these fields in SI units are omitted.

$$\nabla \cdot \mathbf{B} = 0 \qquad i2\pi\rho \cdot \tilde{\mathbf{B}} = 0$$

$$\nabla \times \mathbf{B} = \mathbf{J} \qquad i2\pi\rho \times \tilde{\mathbf{B}} = \tilde{\mathbf{J}}$$

$$\mathbf{B} = \nabla \times \iiint_{-\infty}^{\infty} \frac{\mathbf{J}(\mathbf{r}')}{|\mathbf{r} - \mathbf{r}'|} d^3\mathbf{r}' \qquad \tilde{\mathbf{B}} = \frac{i2\rho \times \tilde{\mathbf{J}}}{\rho \cdot \rho}$$

$$\nabla \times \mathbf{E} = 0 \qquad i2\pi\rho \times \tilde{\mathbf{E}} = 0$$

$$\nabla \cdot \mathbf{J} = 0 \qquad i2\pi\rho \cdot \tilde{\mathbf{J}} = 0$$

All of the above transforms are straightforward except that for the Biot-Savart law, which is shown in appendix A.

The Fourier transformed equations reveal several important properties[1]. *In frequency space, valid electric fields may have only radially oriented vector components.* In other words, because real space electric fields are devoid of curl, their Fourier representations must be purely radial. Similarly, *transformations of magnetic and current fields are allowed only to have vector components which are perpendicular to* ρ. Such vectors lie tangential to the surface of a sphere of radius $|\rho|$, and thus will be referred to as tangential components. Subscripts r and t will denote the Fourier radial and tangential components of a vector field, and as discussed above, certain fields are completely described by one orientation or the other,

$$\tilde{\mathbf{E}} = \tilde{\mathbf{E}}_r, \ \tilde{\mathbf{B}} = \tilde{\mathbf{B}}_t, \text{ and } \tilde{\mathbf{J}} = \tilde{\mathbf{J}}_t.$$

It is standard practice to decompose a real space vector field into its vector components. These could be Cartesian (x,y,z) components or real space radial and tangential (r,θ,φ) components. Naturally, by adding the component vectors together, one recreates the original vector field. Here, vector fields are decomposed into their radial and tangential components in Fourier space. As with real space decomposition, if both of the

---

[1]Dallas, W.J., "Volume Currents in Biomagnetic Imaging", SPIE Vol. 1231 Medical Imaging IV: Image Formation (1990).

Fourier space component fields are inverse transformed separately, a real space summation will reproduce the original function. This method of decomposing a vector field, **F**, into its Fourier components is summarized using the following notation.

$$\mathbf{F} \rightarrow \tilde{\mathbf{F}} = \tilde{\mathbf{F}}_r + \tilde{\mathbf{F}}_t \rightarrow \mathbf{F}_r + \mathbf{F}_t = \mathbf{F}.$$

Producing $\mathbf{F}_r$ will be called a Fourier radial operation. Producing $\mathbf{F}_t$ will be called a Fourier tangential operation. What does the process of performing a Fourier radial or tangential operation actually do? To examine this question, consider that a vector field may be sampled and represented as a sum of delta functions. A coarse sampling typically provides an approximation, but increasing sampling frequency eventually allows reproduction of the field in its original entirety. From this viewpoint, a delta function is the fundamental unit of a vector field, and thus, performing radial and tangential operations on it should provide insight to such operations on entire vector fields.

Consider a delta function **Q** at position $\mathbf{r}_0$ with strength |s|,

$$\mathbf{Q} = \begin{bmatrix} s_x \\ s_y \\ s_z \end{bmatrix} \delta(\mathbf{r} - \mathbf{r}_0).$$

Its Fourier transform is a constant through frequency space modulated by a phase factor dependent upon its real space location

$$\tilde{\mathbf{Q}} = \begin{bmatrix} s_x \\ s_y \\ s_z \end{bmatrix} e^{-i2\pi(\mathbf{r}_0 \cdot \boldsymbol{\rho})}.$$

Projecting this field onto the vectors $\frac{\boldsymbol{\rho}}{|\boldsymbol{\rho}|}$ yields the Fourier radial components

$$\tilde{\mathbf{Q}}_r = \frac{\mathbf{s} \cdot \boldsymbol{\rho}}{|\boldsymbol{\rho}|^2} \boldsymbol{\rho}\, e^{-i2\pi(\mathbf{r}_0 \cdot \boldsymbol{\rho})}.$$

To interpret this result, consider the electric field generated by a dipole described by the same delta function, **Q**;

$$\mathbf{E} = -\nabla\phi \quad \text{with } \phi(\mathbf{r}) = \mathbf{s} \cdot \frac{\mathbf{r}-\mathbf{r}_0}{|\mathbf{r}-\mathbf{r}_0|^3}.$$

Fourier transforming the electric field yields

$$\tilde{\mathbf{E}} = -i2\pi\rho \; F.T.\left\{\frac{\mathbf{s}\cdot(\mathbf{r}-\mathbf{r}_0)}{|\mathbf{r}-\mathbf{r}_d|^3}\right\}.$$

As shown in appendix A,

$$F.T.\left\{\frac{\mathbf{s}\cdot(\mathbf{r}-\mathbf{r}_0)}{|\mathbf{r}-\mathbf{r}_d|^3}\right\} = \mathbf{s}\cdot F.T.\left\{\frac{\mathbf{r}-\mathbf{r}_0}{|\mathbf{r}-\mathbf{r}_d|^3}\right\} = \mathbf{s}\cdot\frac{-2i\rho}{|\rho|^2}e^{-i2\pi(\mathbf{r}_0\cdot\rho)}.$$

Therefore, the transform of the electric dipole field is

$$\tilde{\mathbf{E}} = -4\pi\rho\,\frac{\mathbf{s}\cdot\rho}{|\rho|^2}e^{-i2\pi(\mathbf{r}_0\cdot\rho)},$$

and is equal to the Fourier radial projection of a delta function

$$\tilde{\mathbf{E}} = -4\pi\tilde{\mathbf{Q}}_r \rightarrow \mathbf{E} = -4\pi\mathbf{Q}_r.$$

Fourier radial operation on a delta function produces a real space vector field which is proportional to the field generated by a dipole at the same location.

Remember that a dipole moment is directed toward the positive electric pole which is opposite to the actual electric field. Radial operation on a similarly oriented delta function requires the negative sign and to provide the true field direction.

Below is a series of planar slices through three-dimensional vector fields that illustrates fourier projection operation. Figure (2.1) presents the initial delta function s = (1,0,1) at position (8,8,8). The border is the edge of the discrete space 16x16x16 voxels.

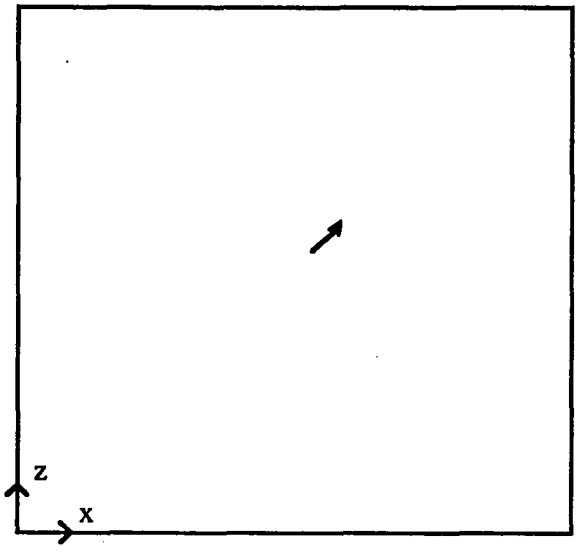

Figure (2.1): A delta function in real space, plane y = 8.

Next is the real part of Fourier transform plane $\eta = 0$. Since the dipole was away from the origin, a phase factor modulates the otherwise constant vector field.

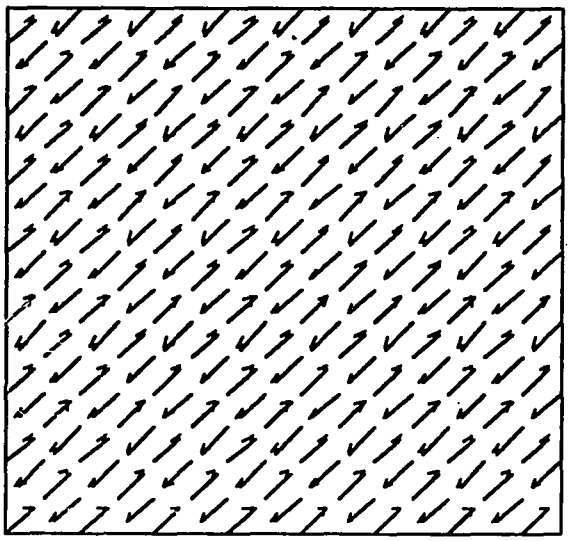

Figure (2.2): Real part of delta function Fourier transform, plane η=0.

A radial projection yields

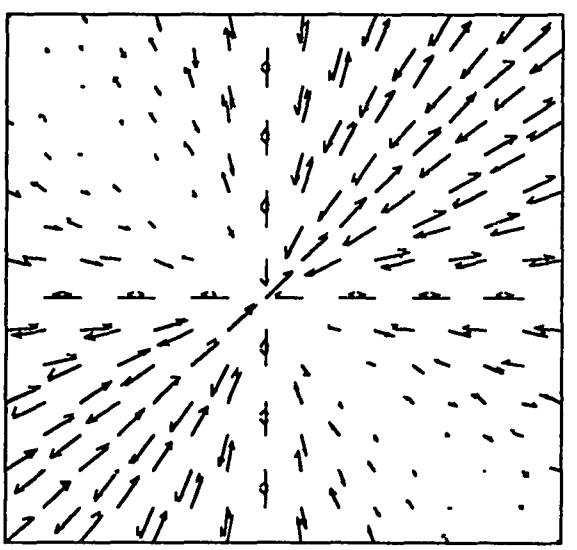

Figure (2.3): The radial components of the delta function Fourier transform, real part of plane η=0.

Finally, inverse Fourier transforming the radial components produces an electric dipole field. Because the dipole is a singularity whose field decreases as $|r|^{-3}$, a vector graph that contains the dipole itself is dominated by the field strength at and very close to the dipole's location. Therefore, for better detail, two views of the dipole field are presented -- one that includes the dipole moment and one taken some distance away. Figure (2.4) presents the plane y=8 now containing an electric dipole field in place of the original delta function. Notice that the external vectors oppose the flow of the central dipole moment, so the curl is zero everywhere. The electric dipole field is so named because it describes the electric field that results when positive and negative point charges are brought close together. Imagine that the central value in figure (2.4) points from a hypothetical positive charge to a negative charge.

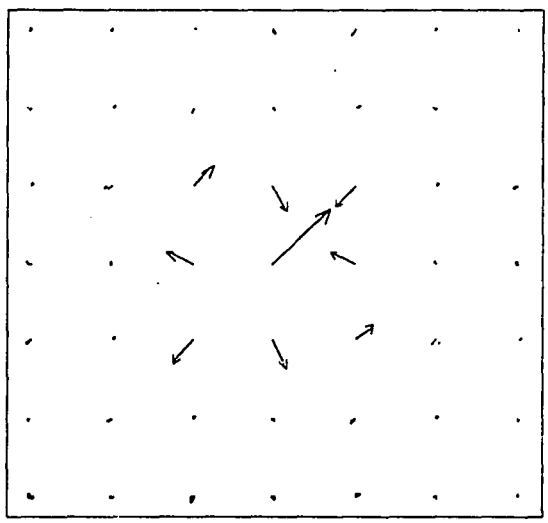

Figure (2.4): The electric dipole field, plane y=8.

Figure (2.5) is a second vector slice of the same dipole field. However, the slice passes several planes away from the dipole moment in order to capture the form of the return field which at this distance, is many times weaker than the dipole moment.

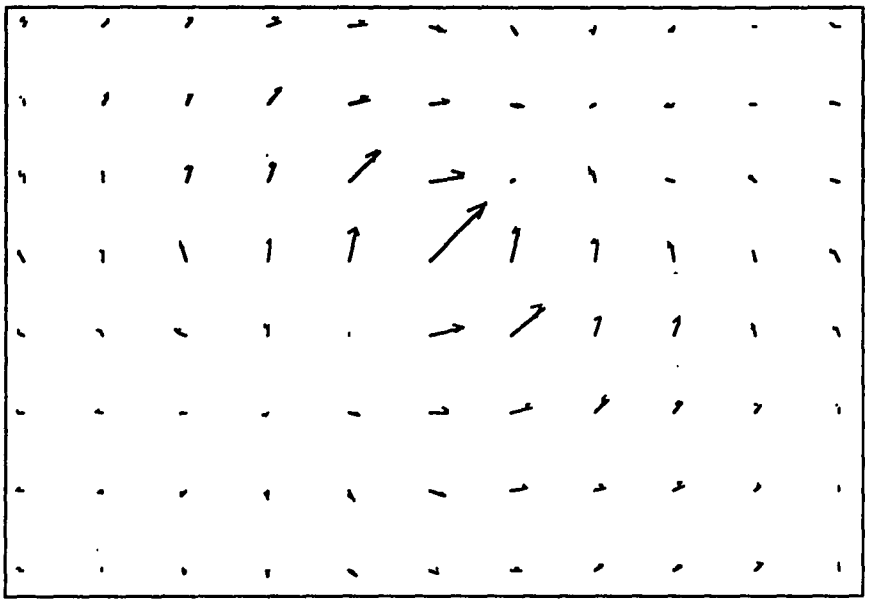

Figure (2.5): The return field of the electric dipole, plane y=5.

Next, examine how a Fourier tangential operation differs from the Fourier radial operation. Figure (2.6) is the tangential projection of the Fourier transform of the original delta function.

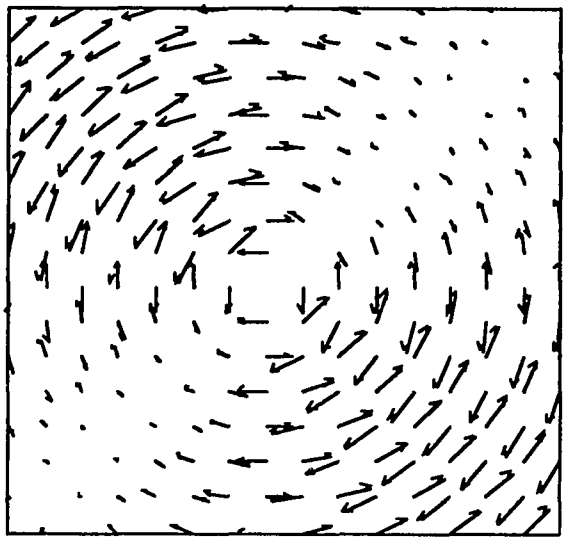

Figure (2.6): The real part of the tangential projection of the Fourier transform of the delta function, plane η=0.

Inverse Fourier transformation of the tangential projection creates a current dipole -- identical to the electric dipole except that the field external to the current dipole source is inverted. The current dipole field lines flow with the direction of their source to eliminate any roots of divergence.

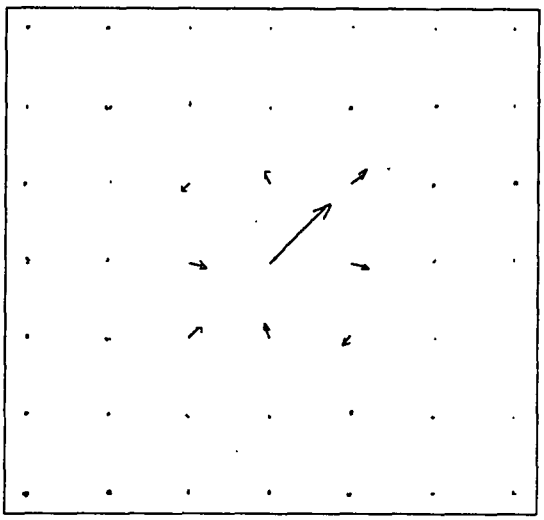

Figure (2.7): The current dipole generated by a Fourier tangential operation on a delta function, plane y=8.

Finally, figure (2.8) displays the external field of the current dipole. This is the same plane as figure (2.5). Again, note that the field lines have the same magnitude as, but are directed oppositely to, the field lines of the electric dipole in figure (2.5).

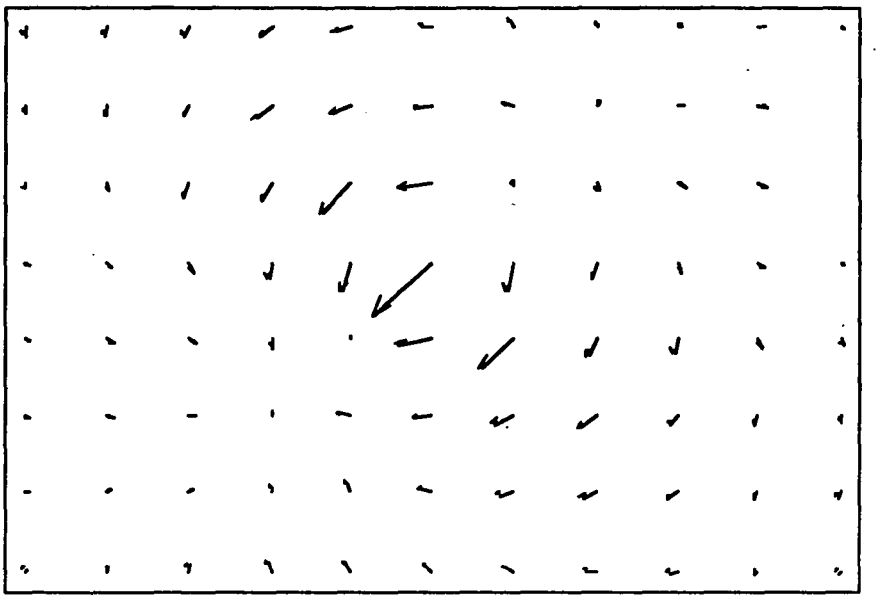

Figure (2.8): The current dipole return field, plane y=5.

Together, the current and electric dipole fields sum to reproduce the original delta function, $\delta_r(\mathbf{r}) + \delta_t(\mathbf{r}) = \delta(\mathbf{r}_0)$. Realize that the two dipole field types are equal but opposite to each other away from the source. ***Externally, both fields have zero curl and zero divergence.*** The electric dipole field has zero curl everywhere and divergence only at its source. In contrast, the current dipole field has zero divergence everywhere and curl only at its source.

Chapter 3

The Volume Current Problem

The concepts developed above are powerful tools for solving of a variety of boundary value problems encountered in electrostatics and magnetostatics. In this chapter and the next, several numerical algorithms utilizing Fourier projection operations will be presented. To begin, consider the problem of calculating volume currents[1]. Given a volume of arbitrary but known conductivity that contains one or many dipole current sources (delta functions), how will the ohmic currents distribute themselves throughout the conducting volume?

The total current density **J** is the sum of the impressed current sources $\mathbf{J}_i$ and the Ohmic response current $\mathbf{E}\sigma$.

$$\mathbf{J} = \mathbf{J}_i + \mathbf{E}\sigma$$

For quasistatic conditions, no divergence of the total current density is allowed, and the electric field may be described by the negative gradient of its scalar potential V.

$$\nabla\cdot\mathbf{J} = 0 \qquad \mathbf{E} = -\nabla V$$

Because the divergence of the total current is zero, the divergence of the volume (Ohmic) current must be equal but opposite to the divergence of the impressed sources,

$$\nabla\cdot(\sigma\nabla V) = \nabla\cdot\mathbf{J}_i.$$

The impressed sources and the conductivity configuration are known, so the goal is to solve the above equation for V, which will give **E**, and thus predict the distribution of the volume current $\mathbf{E}\sigma$.

In regions of constant, non-zero conductivity, σ may be extracted from the divergence term to produce the well-known Poisson equation, $\Delta V = \nabla\cdot\mathbf{J}_i/\sigma$. If all space is filled with a constant conductivity, one need only solve the Poisson equation to determine

---

[1] Sarvas, J. Basic mathematical and electrical concepts of the biomagnetic inverse problem. Phys. Med. Biol., 1987 Vol. 32, No. 1, 11-22.

the volume current density everywhere. For a single delta function impressed source $\mathbf{Q}\delta(\mathbf{r}-\mathbf{r}_0)$, the solution to the Poisson equation is, not surprisingly, an electric dipole potential,

$$V(\mathbf{r}) = \frac{1}{4\pi\sigma}\,\mathbf{Q}\cdot\frac{\mathbf{r}-\mathbf{r}_0}{|\mathbf{r}-\mathbf{r}_0|^3}.$$

The delta function source and the electric dipole response add to produce a total current density that is a current dipole field. However, if the conductivity is not homogeneous, solving for the electric potential becomes considerably more difficult.

Realize that the volume currents need to be determined in order to calculate the magnetic field generated by an impressed source in conducting media. In 1967, Geselowitz[1] showed that, for piecewise constant conductivity patterns, the volume current contribution to the external magnetic field may be calculated from a knowledge of the electric potential at each interface between regions of different conductivity. He derived a surface integral equation,

$$\frac{\sigma_k'+\sigma_k''}{2}V(\mathbf{r}) = \sigma_n' V_0(\mathbf{r}) - \sum_{j=1}^{n}\frac{\sigma_j'+\sigma_j''}{4\pi}\int_{S_j} V(\mathbf{r}')\mathbf{n}(\mathbf{r}')\cdot\frac{\mathbf{r}-\mathbf{r}'}{|\mathbf{r}-\mathbf{r}'|^3}\,dS_j.$$

that requires an iterative search for self-consistent solutions for the potentials along every surface, S_j. Altogether, there are n regions of different conductivity (perhaps arranged as concentric shells). The impressed source is in region n, and V_0 is the potential that would be generated by that source in an infinite homogeneous conducting medium. σ' is the conductivity to the inside of an interface, and σ'' is the conductivity to the outside. Calculating the potential over surface k (k=1 to n) requires a summation of surface integrals over the potential at all surfaces. Initially, the electric potential at every surface is unknown, so guesses must be provided for each surface to start the iteration.

Although it is presently the most common approach to solve the volume current problem, the Geselowitz solution suffers from a number of drawbacks. It is restricted to piecewise constant conductivity configurations; it is difficult to program; and it has discontinuities in every kth integrand that can cause numeric instability. As an alternative, a

---

[1]Geselowitz, D.B. Biophys. J., 1967 Vol 7, pp. 1-11.

novel Fourier technique is presented below that solves the volume current boundary value problem more generally, faster, and with easier computer implementation.

The Volume Current Algorithm

An outline of the algorithm is the following --

Step I: Perform a Fourier tangential operation on the present estimate for the total current density **J**. (The initial **J** is the given $\mathbf{J}_i$)

Step II: Check for convergence. (Has Fourier tangential operation altered the estimate for **J** from the previous iteration? If not, the solution is found.)

Step III: Confine current to regions of nonzero conductivity. (Not a critical step, but it will speed convergence)

Step IV: Calculate an estimate for the electric field using $\mathbf{E} = (\mathbf{J}-\mathbf{J}_i)/\sigma$. (The electric field in regions of zero conductivity is set equal to its value from the previous iteration. For the zeroth iteration, it is kept equal to zero)

Step V: Perform a Fourier radial operation on the electric field.

Step VI: Calculate a new estimate for the total current density using $\mathbf{J} = \mathbf{J}_i + \mathbf{E}\sigma$.

Step VII: Return to Step I.

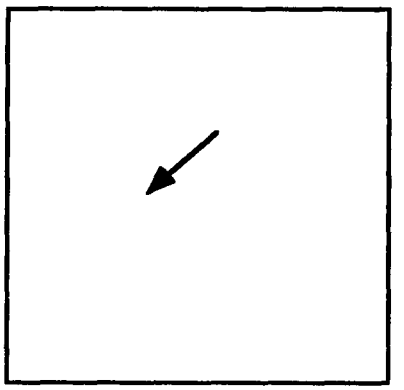

Ji

Figure 3.1

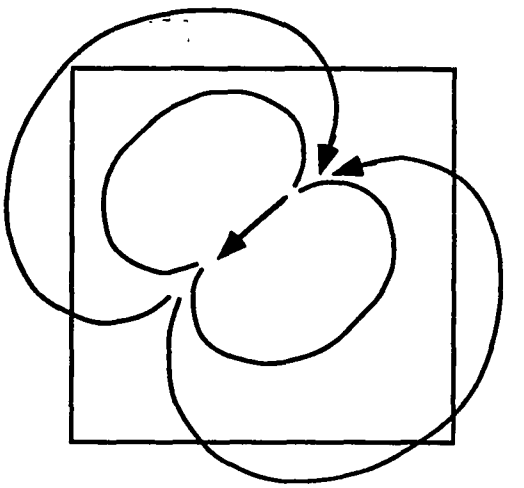

J tangential

Figure 3.2

To begin, the algorithm requires data matrices for the conductivity and the current sources. Although, the algorithm will operate on any contiguous conductivity configuration and on any number of current sources, a simple case will be used for explanation. Figure 3.1 depicts a single delta function placed within a three-dimensional box of non-zero conductivity. Outside of the box, the conductivity is zero. As shown in figure 3.2, a Fourier tangential operation produces the zeroth order estimate for the total current density. This operation replaces the delta function with its associated current dipole field. Remember that this field is correct for homogeneous conductivity configurations. However, most situations demand that current be confined to a finite region. Figure 3.2 indicates that the isotropic estimate for volume currents is not the solution since current is found beyond the walls of the volume.

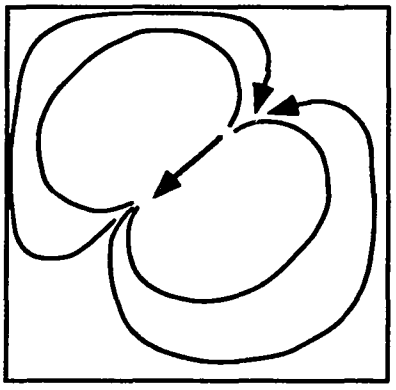

Confine Current

Figure 3.3

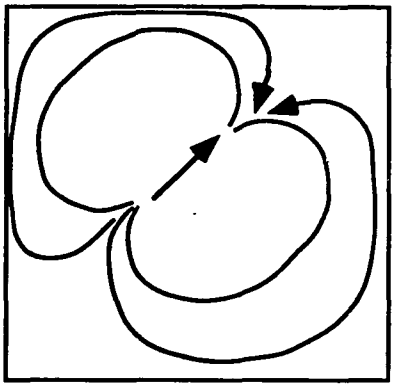

$E = (J - Ji)/\sigma$

Figure 3.4

Because being confined to a finite region is the most significant change to the current paths from their zeroth order solution, the speed of convergence for the algorithm is improved by implementing a simple subloop that confines the currents. Recall that valid current fields have zero divergence everywhere and thus have only tangential components in reciprocal space. By simply removing current density external to the conducting volume, the interior field that remains would no longer be a valid current field; it would have sources of divergence over the surface of the volume.

A better approach is to remove the external current density in a manner that maintains the tangential nature of the interior field. One method is to subtract, not the entire external field from the original, but just the Fourier tangential part of the external field. Subtracting a tangential external field from the original tangential field produces a new estimate which is still tangential or divergenceless. A second method, which requires less computation, is to set the external field to zero and keep the Fourier tangential part of the internal field. Again, the magnitude of the external current density is significantly reduced while the new estimate remains tangential.

It is perhaps a little surprising that both current confinement methods are mathematically equivalent. To see this, let the field external to the conducting volume be

B, the interior field **A**, and the total current field (which is tangential) **C**. Naturally, adding the inner field to the outer field produces the entire field.

$$\mathbf{A} + \mathbf{B} = \mathbf{C}_t$$

Decomposing fields **A** and **B** into their Fourier component parts demonstrates that the Fourier radial part of **A** must be equal and opposite to the Fourier radial part of **B**.

$$(\mathbf{A}_r + \mathbf{A}_t) + (\mathbf{B}_r + \mathbf{B}_t) = \mathbf{C}_t \quad \rightarrow \quad \mathbf{A}_r = -\mathbf{B}_r$$

or

$$\mathbf{C}_t - \mathbf{B}_t = \mathbf{A}_t.$$

Therefore, subtracting the tangential part of the outer field from the original produces the same result as simply keeping the tangential part of the inner field.

Performing a Fourier radial (tangential) operation on a field replaces each vector within that field with its corresponding electric (current) dipole field. Therefore, although field **A** is spatially confined in real space, its Fourier component fields in general are not. By construction, field **A** is zero external to the conducting volume. Consequently, its Fourier radial and tangential component fields must cancel each other in this region. Outside of the volume, $\mathbf{A}_r$=-$\mathbf{A}_t$. This result is consistent with the fact that the electric and current dipole fields are equal but opposite everywhere except their source. $\mathbf{A}_r$ is the superposition of the electric dipole fields generated by **A**. $\mathbf{A}_t$ is the superposition of the current dipole fields generated by **A**. Since **A** has non-zero vectors only within its region, it provides dipole sources only within its region. The electric dipole fields generated by those sources will be exactly opposite to the current dipole fields generated by those sources in regions not containing any sources. As required, the fields $\mathbf{A}_r$ and $\mathbf{A}_t$ will sum to zero at all points external to region **A**.

Initially, $\mathbf{A}_t$ will not be spatially confined. However, repeating the confinement operation several times will reduce the external values to relatively insignificant strengths. Eventually, field **A** becomes both spatially confined and Fourier tangential. An example of such a field is a simple current loop. It is spatially confined and has no divergence.

Figure 3.3 is a spatially confined version of the zeroth order current estimate in figure 3.2. It appears to be a very reasonable solution to the volume current problem.

However, there is no guarantee that it is correct unless another constraint is satisfied. The electric field associated with the volume current paths must have no sources of curl. The electric field is calculated using $\mathbf{E} = (\mathbf{J}-\mathbf{J}_i)/\sigma$. To avoid a division by zero in regions external to the conducting volume, the electric field from the previous iteration is inserted for those regions. Figure 3.4 shows the electric field for the zeroth iteration. This invalid electric field has non-zero curl across the surface of the volume and will also have internal curl if the volume contains heterogeneous conductivity patterns.

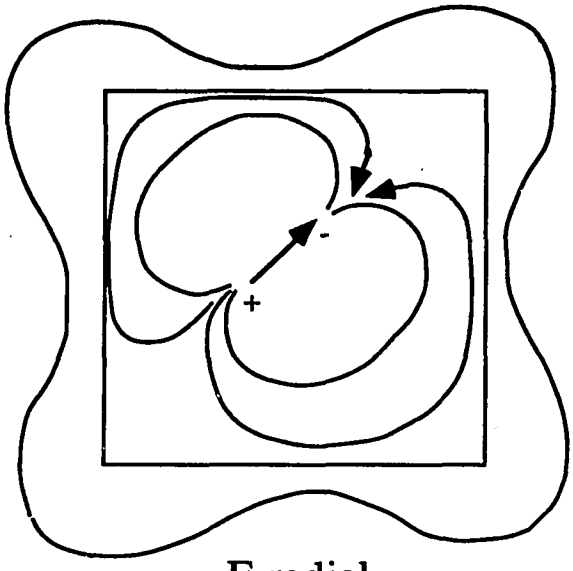

E radial

Figure 3.5

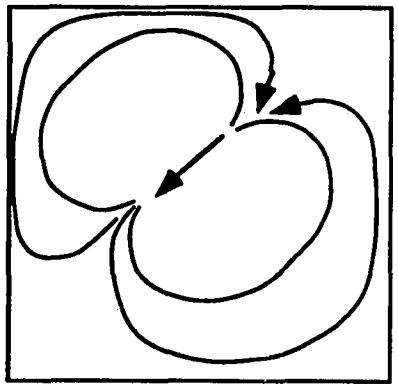

$J = Ji + E\sigma$

Figure 3.6

As shown is figure 3.5, a Fourier radial operation removes curl from the electric field, and for the zeroth iteration, generates an estimate for the external field. The conducting volume has forced the creation of new sources for electric field. In order to confine volume currents, or preferentially maneuver them to paths of high conductivity, electric charge was amassed at regions of non-zero conductivity gradient, such as at the surface of the volume.

$$\nabla \cdot E = \nabla \cdot \frac{J_v}{\sigma} = J_v \cdot \nabla \frac{1}{\sigma} + \frac{1}{\sigma} \nabla \cdot J_v$$

$$\nabla \cdot E = J_v \cdot \nabla \frac{1}{\sigma}$$

For regions not containing current sources, the divergence of E (the location of charge) is non-zero only where the gradient of $1/\sigma$ is non-zero.

One might be concerned that future Fourier radial operations, on a field with vectors now external to the volume, have the potential to introduce divergence in the external region. However, the algorithm will never add divergence to the external field since the zeroth iteration estimate is generated by vector electric dipole sources located within the conducting volume; therefore, the external electric field will have both zero divergence and zero curl. For the next iteration, keeping the zeroth order estimate for the external field forces new sources to arise only internally at locations demanded by the altered internal current paths. Since all perturbations to the zeroth iteration solution are internal, so are any new sources for divergence.

Figure 3.6 displays the next step of the algorithm; recalculate the total current field using $\mathbf{J}=\mathbf{J}_i+\mathbf{E}\sigma$. If any changes to the electric field were created by the Fourier radial operation, the new estimate for $\mathbf{J}$ will differ from the previous iteration. However, the electric field alterations may have introduced divergence to the new current field; therefore, the new current field must be returned to step I for Fourier tangential treatment. The algorithm continues until it generates a new current density estimate that is essentially equivalent to the current field from the previous iteration. In order for this to happen, the current field must purely Fourier tangential, while at the same time, its associated electric field must be purely radial. For a given set of conductivity boundary conditions and impressed sources, by the construction of the problem, only the uniquely correct solution can satisfy both of those conditions.

Although understanding this algorithm is challenging, implementing it is almost easy. With a little thought about the physical conditions that need to be satisfied, and the magic of Fourier transformation, the volume current problem practically will solve itself. Experience indicates that the above algorithm converges rapidly (fewer than ten iterations), but the ultimate accuracy is determined by the resolution of the discrete Fourier transform

implemented. More on discrete Fourier transform approximations will be discussed toward the end of this chapter.

Direct calculation for a dipole in a half-space

Verifying the results of the volume current algorithm is difficult because closed-form solutions to the problem exist for only a few special geometries. Since the Geselowitz formulation uses an implicit solution for the volume currents to calculate the magnetic field external to a conducting body, the results of the Fourier algorithm are converted to a magnetic field using the Biot-Savart law. A simple problem to consider is a vertical dipole placed in a half-space of constant conductivity. The rather lengthy calculation using the Geselowitz formulae is presented in appendix B. This particular example is useful as a means to compare numeric with analytic results because the return currents generated by this configuration contribute a magnetic field beyond the volume which exactly cancels the field generated by the impressed current.

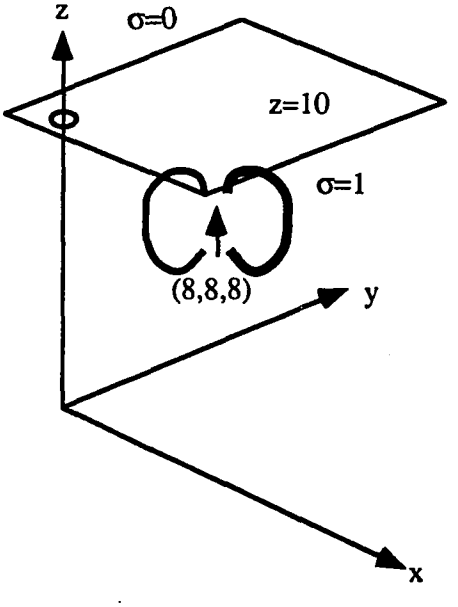

Figure 3.7: A vertical dipole at position (8,8,8). The conductivity is zero above the plane z=10 and one below.

Figure 3.8 is an example of the electric field generated by the volume current algorithm to solve the problem shown in figure 3.7. Notice the divergence at the interface caused by a distribution of positive charge collected to repel volume currents back into their half-space.

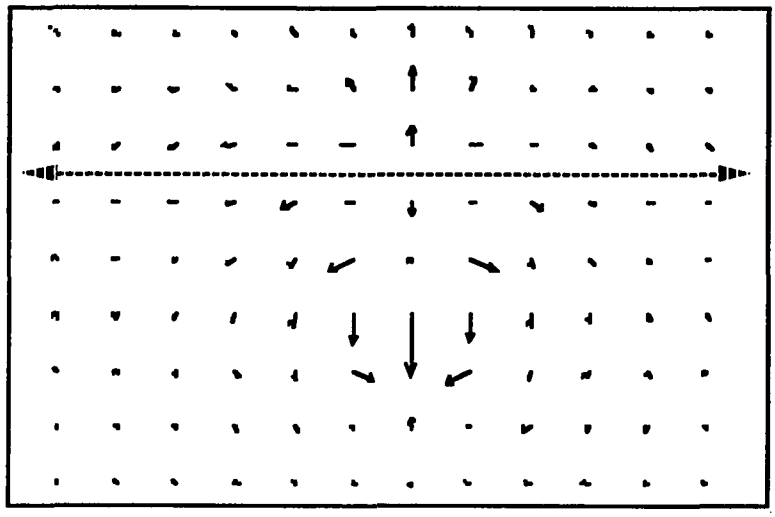

Figure 3.8: The electric field in plane y=10. The dotted line indicates the interface between zero and non-zero conductivity.

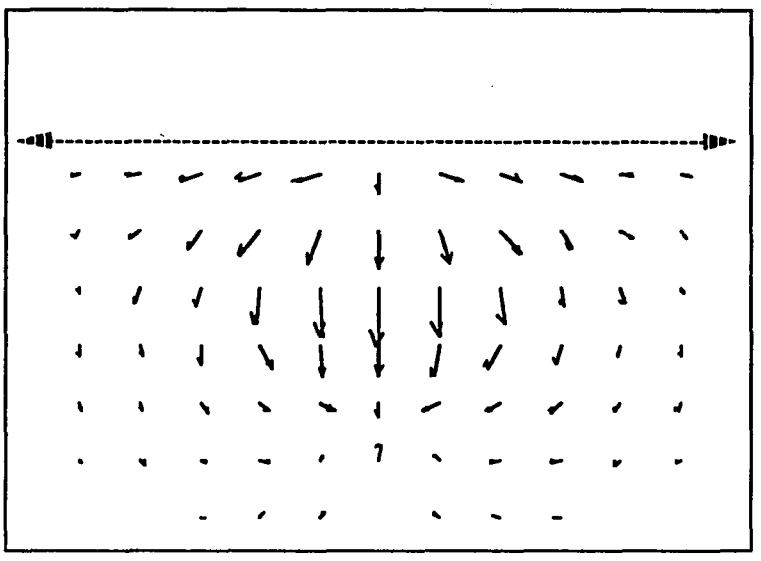

Figure 3.9: The current field in plane y=12.

Figure 3.9 shows the current field in plane y=12, while figure 3.10 offers a birds-eye view of the surface current at plane z=10.

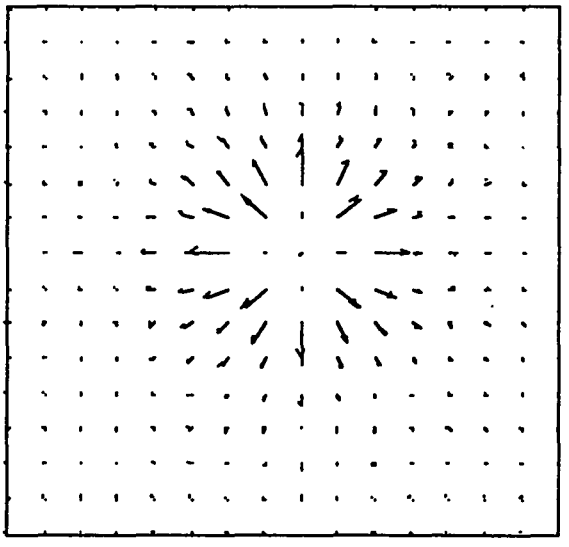

Figure 3.10: The top surface currents, plane z=10.

Finally, figure 3.11 presents the predicted magnetic field in plane y=10. The lateral vectors in this side view are part of the field lines encircling the vertical dipole. Notice that, as required, the magnetic field has nearly disappeared above the plane. The residual field is small and may be attributed to error introduced by using a 16x16x16 matrix to represent infinite space.

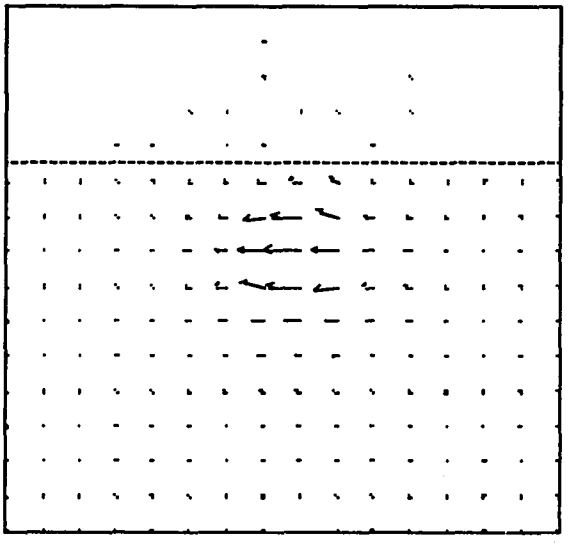

Figure 3.11: The magnetic field in plane y=6. Ideally, the field should equal zero above the plane z=10.

Direct calculation for a dipole in a sphere

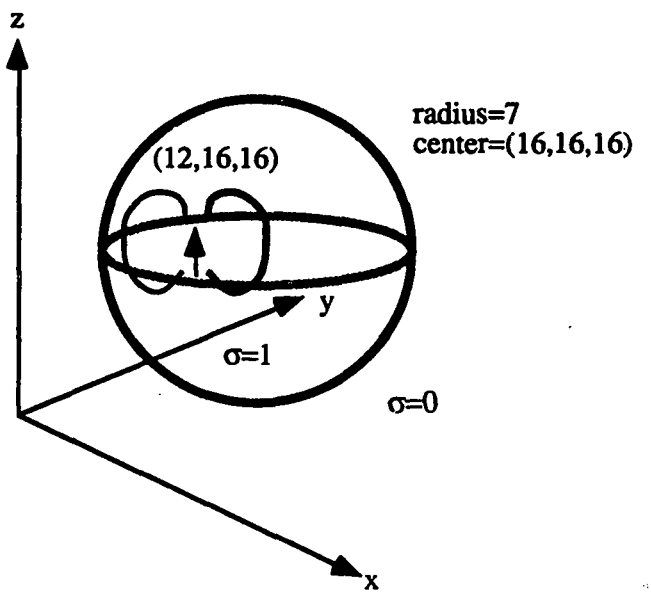

Figure 3.12: A vertical dipole in a sphere of uniform conductivity.

A radially symmetric conductivity is the only other configuration for which an analytic solution to the volume current problem exists. The exterior magnetic field[1] created by a dipole **Q** at position $\mathbf{r}_0$ within a sphere centered at the origin is

$$\mathbf{B} = \frac{a(ar+r^2-(\mathbf{r}_0\cdot\mathbf{r}))(\mathbf{Q}\times\mathbf{r}_0) - ((\mathbf{Q}\times\mathbf{r}_0)\cdot\mathbf{r})((\frac{a^2}{r}+\frac{\mathbf{a}\cdot\mathbf{r}}{a}+2r+2a)\mathbf{r}-(a+2r+\frac{\mathbf{a}\cdot\mathbf{r}}{a})\mathbf{r}_0)}{4\pi a^2(ar+r^2-\mathbf{r}_0\cdot\mathbf{r})^2}$$

where $\mathbf{a} = \mathbf{r}-\mathbf{r}_0$, $r=|\mathbf{r}|$, and $a=|\mathbf{a}|$.

This expression is valid only for regions external to the conducting sphere. The magnetic field is independent of $\sigma(r)$. To appreciate the degree of field alteration induced by

[1] Sarvas, J. Basic mathematical and electrical concepts of the biomagnetic inverse problem. Phys. Med. Biol., 1987 Vol. 32, No. 1, 11-22.

confining the volume currents, recall that the field generated by the same dipole in homogeneous conductivity is simply

$$\mathbf{B} = \frac{Q \times a}{4\pi a^3}.$$

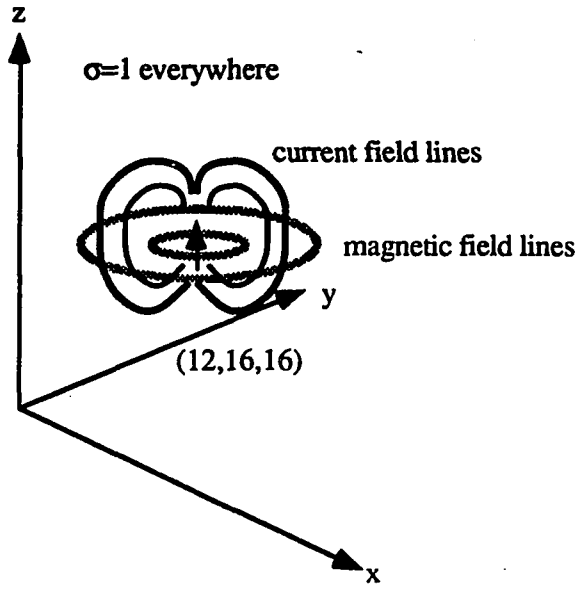

Figure 3.13: A vertical dipole at position (12,16,16) surrounded by an infinite space of uniform conductivity.

The Fourier volume current algorithm was used to solved the problem shown in figure 3.12. Again, the algorithm first solved for the total current distribution and then used that solution to generate a magnetic field for comparison with the analytic solution given above. Figures 3.14 - 3.16 present three different views of both the simulated magnetic field and the analytic solution. Also, for each view, the magnetic field generated by the dipole in Figure 3.13 is presented to emphasize the degree of alteration induced by spherical confinement. The circles drawn in parts B) and C) of each figure are projections of the maximum circumference of the sphere which lies tangential to these planes of view.

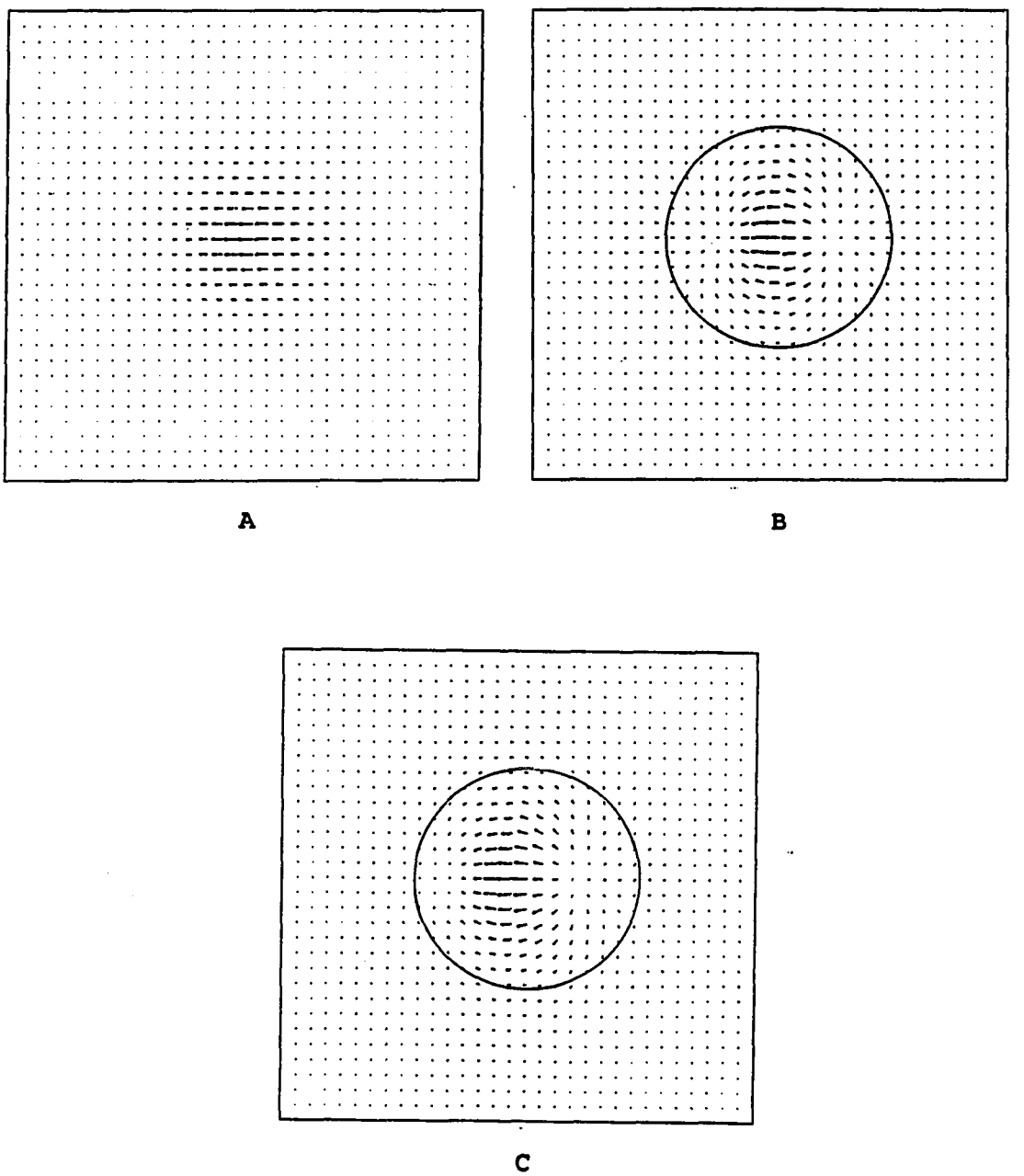

Figure 3.14: Plane x=8 of the magnetic field generated by: A) the analytical solution to the problem in Fig. 3.13 B) the analytical solution to the problem in Fig. 3.12 C) the simulated solution to the problem in Fig. 3.12.

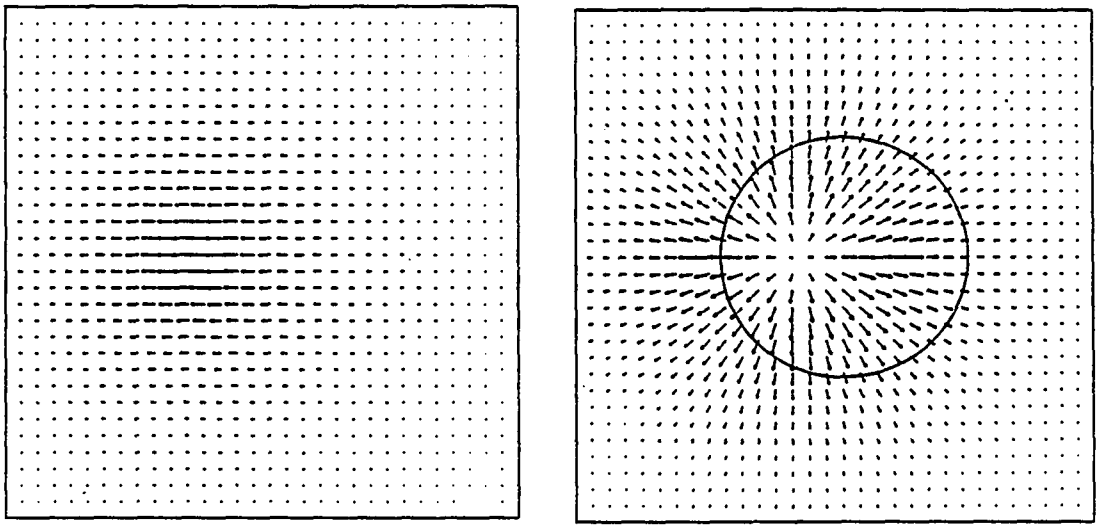

A

B

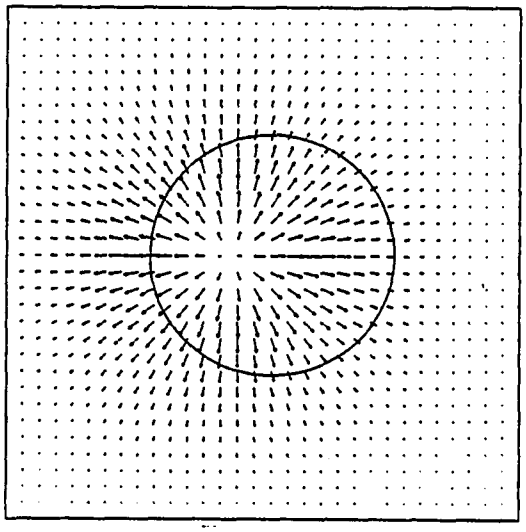

C

Figure 3.15: Plane y=24 of the magnetic field generated by: A) the analytical solution to the problem in Fig. 3.13 B) the analytical solution to the problem in Fig. 3.12 C) the simulated solution to the problem in Fig. 3.12.

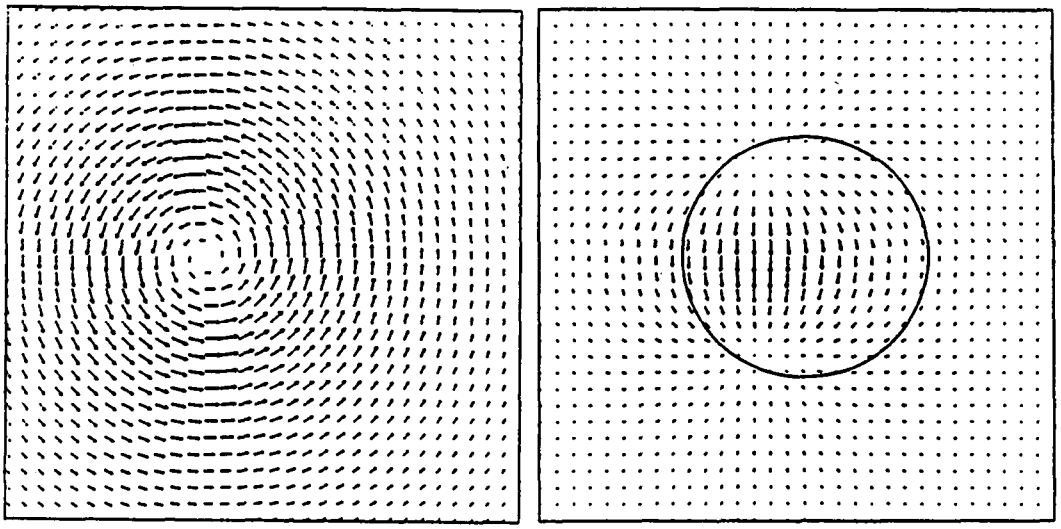

A B

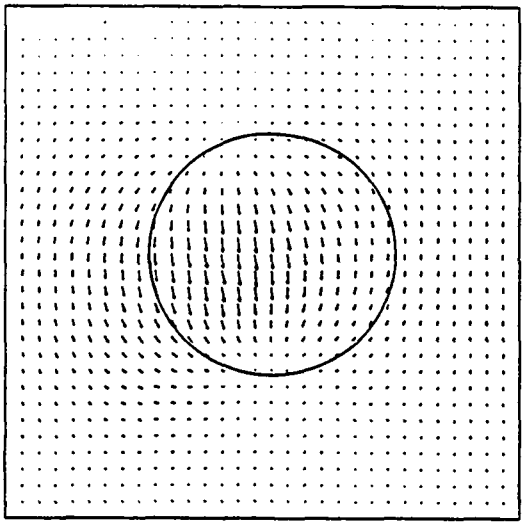

C

Figure 3.16: Plane z=8 of the magnetic field generated by: A) the analytical solution to the problem in Fig. 3.13 B) the analytical solution to the problem in Fig. 3.12 C) the simulated solution to the problem in Fig. 3.12.

The results shown in Figures 3.14 - 3.16 demonstrate how Fourier projection techniques are able to generate reasonably accurate predictions for the external magnetic field. However, the match with the analytic solution is not perfect because a cluster of four delta functions arranged in a square of voxels was used to simulate the single delta function assumed for the analytic calculation. Because the cluster extended one voxel towards the center of the sphere, the simulated solution is shifted slightly with respect to the analytic solution. Also, as is especially apparent in Figures 3.14 and 3.16, the field from the simulated cluster is a slightly broadened version of the analytic solution.

The cluster was used in place of a single delta function to counter problems introduced by discrete Fourier transformation. For periodic or spatially smooth functions, the discrete Fourier transform can be a good approximation to the integral Fourier transform. Unfortunately, the delta function, or dipole field for that matter, does not qualify as periodic or smooth. Indeed, it is formed by summing equal contributions from every spatial frequency to infinity. Analytically, Fourier radial operation on a delta function produces a dipole field. In practice, however, the finite frequency components have difficulty reproducing certain regions of a proper dipole field. As Figure 3.17 illustrates, a discrete Fourier radial operation on a delta function reproduces a dipole field quite accurately away from the source, where the field is much smoother.

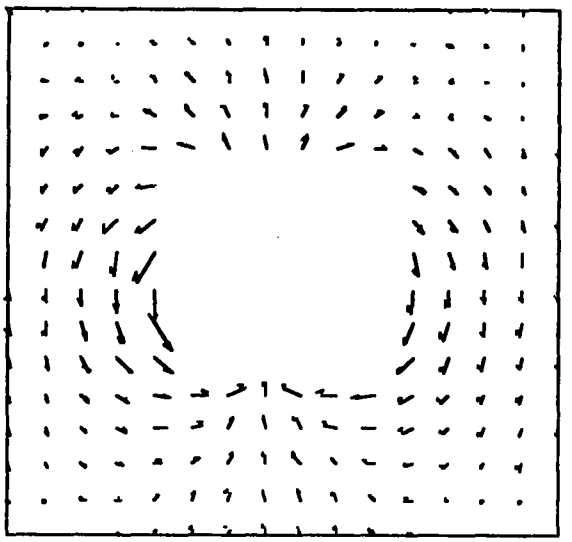

Figure 3.17: The dipole field generated by a Fourier radial operation. The plane of view is located several voxels away from the source. The central values have been removed to emphasize remote structure.

In contrast, planes of view that pass through the dipole source contain the part of the field made of very high spatial frequencies. Figure 3.18 shows how discrete Fourier transformation has significantly more difficulty properly generating the field in planes near the dipole source.

Using a cluster of delta functions for the source provides a smoother field for Step I of the volume current algorithm. This helps to eliminate "ringing" effects generated by a single delta function source. Although the clustered sources produce a noticeable smoothing in the magnetic field, Figures 3.14 - 3.16 show that form and features of the field emerge quite faithfully. In principle, Fourier projection techniques could provide great accuracy. However, finite sampling and discrete Fourier transforms typically force one to accept smoothing effects.

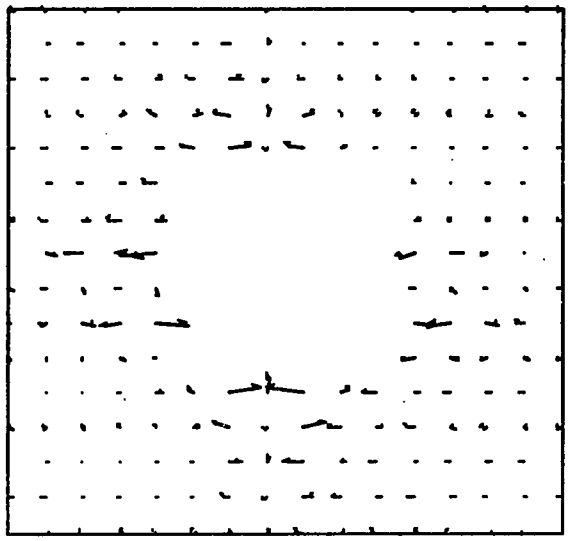

Figure 3.18: The poor results that a discrete Fourier radial operation produces for the field in the plane of the dipole source. The central values have been removed to emphasize remote structure.

On the bright side, Fourier projection techniques are impressive at rapidly producing reasonable field estimates for difficult boundary value problems. Simple tricks, such as, using the analytic expression for dipole fields to produce the zeroth order solutions in Step I, can improve performance even further. In general, the Fourier projection algorithm performs better on a collection of smoothly varying dipoles than isolated delta functions. Although much slower and difficult to implement, finite difference or finite element routines will probably offer greater accuracy. However, the likelihood and speed of convergence for such routines is enormously dependent upon good initial estimates. Therefore, when accuracy is critical, one could easily create a hybrid routine combining the speed of the Fourier with the accuracy of the finite difference routines.

Chapter 4

Magnetic Field Extrapolation

Chapter 3 presented a means to calculate the total electric current generated by sources located in a body with arbitrary conductivity configuration. A simple calculation can convert these electric currents to a magnetic field; this is known as the forward problem. The inverse problem is to reproduce the current paths from a measurement of magnetic field values external to the body. As discussed in chapter 1, the inverse problem is not uniquely solvable, and additional constraints are needed to promote desired solutions. This chapter demonstrates how Fourier projection techniques may be use to solve magnetic boundary value problems and suggests how the technique provides a unique environment in which to apply inverse problem constraints.

The equations describing static magnetic fields are much the same as those which describe electric fields, but the roles of curl and divergence are reversed. Until a monopole is discovered, static magnetic fields will have zero divergence everywhere and curl only at locations containing electric current. Imagine that all current sources are known to be contained within a finite volume, the skull for example, and that the magnetic field generated by these sources is known over the surface of the volume. What knowledge can be acquired of the magnetic field for the rest of space? External to the volume, the problem is well-posed. In the absence of sources, a magnetic scalar potential may be introduced, and the problem is characterized by the Laplace equation with Neumann boundary conditions. The solution is unique, but there exists no generally accepted means to solve this problem.[1] Typically one must choose between a finite difference or a finite element scheme; neither of which is very fast or easy to program. As an alternative, consider the following solution based on the Fourier radial operation.

The Laplace equation is $\nabla^2\mu = 0$, where μ is the magnetic scalar potential. For the Laplace equation to have a unique solution, the Neumann boundary conditions require that the normal derivative of μ be known over a closed surface. Or, since $\mathbf{B} = -\nabla\mu$, it is sufficient to know the magnetic field over a closed surface. A Fourier radial operation on a

[1]Steele, C.W. Computation of Magnetic and Electric Fields, Wiley Interscience, 1988.

surface of magnetic field measurements generates the zeroth order estimate for the external magnetic field.

The Fourier radial operation replaces the input field with a superposition of electric dipole fields that have zero curl everywhere and divergence only at their sources. Since no sources were present external to the volume before the radial operation, any resultant external field necessarily has zero curl beyond and divergence only at the surface. The unique solution to the Laplace equation is a field with zero curl and zero divergence that matches the required values over a closed surface. A single radial operation almost generates this field but fails to guarantee that the surface input values remain unchanged. A superposition of electric dipole fields will not in general leave the source values unchanged.

The difference between the known surface values and the surface values altered by the radial operation becomes the input to the next iteration. A Fourier radial operation is performed on the surface difference values, and the resultant field is added to the original. The unique solution to the Laplace equation is achieved when the magnetic field at the surface remains unchanged by a radial operation. Naturally, the Fourier operation will calculate field values for all space. As a whole, however, the magnetic field cannot have any divergence, so the internal part of the solution is necessarily invalid and must be ignored.

Figure 4.1 shows a current loop phantom source located slightly off-center one-third above the bottom of a cubical volume. The current loop produces a magnetic dipole field that exits the top of the volume and curls around to reenter the bottom. The magnetic field mapping system described in chapter one was used to collect a surface of field measurements shown in Figure 4.2.

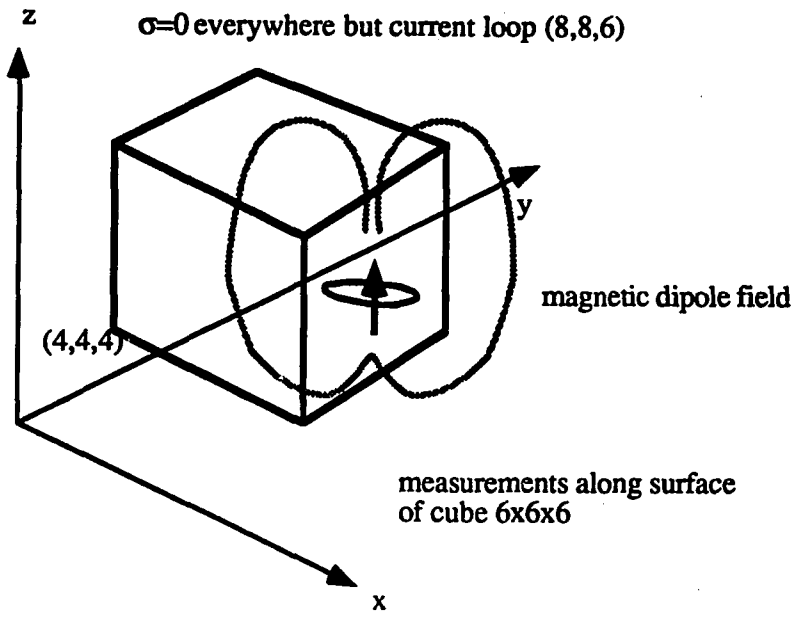

Figure 4.1: A current loop phantom source generating a magnetic dipole field that was mapped over the surface of the cube.

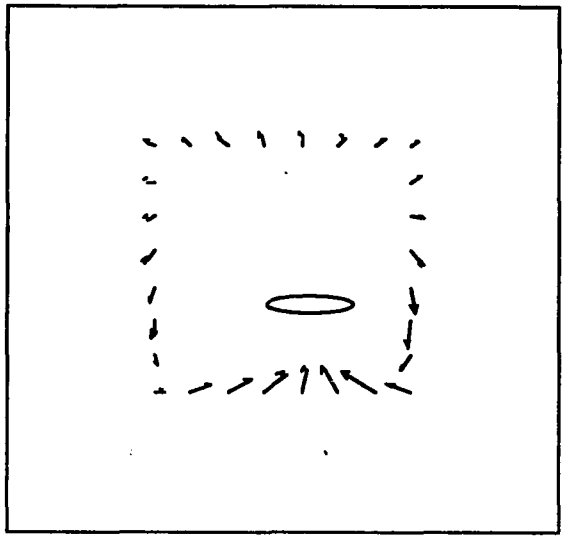

Figure 4.2: Plane y=8 of the surface magnetic data collected from the source in Fig. 4.1. Plane y=8 cuts through the center of the current loop shown here as an oval. (From this perspective it should actually look like a line segment).

Figure 4.3 shows the result of Fourier radial iteration on the surface data. The invalid internal field has been set to zero.

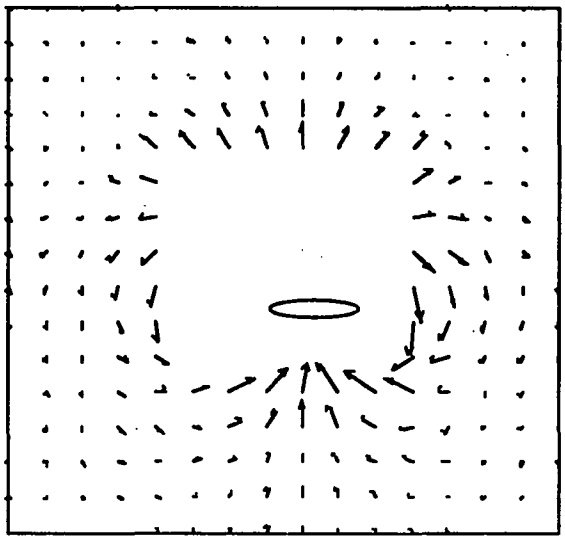

Figure 4.3: Plane y=8 of the external magnetic field generated by a Fourier radial iteration algorithm.

Notice that the Fourier radial operations performed a reasonably correct extrapolation of the surface data by filling out the form of a magnetic dipole field. Smoothing effects from the discrete Fourier transform cause the solution to deteriorate near the edges of the vector space.

The 32x32 pixel graphs in Figure 4.4 illustrate how the quality of algorithm performance generally improves when larger 3-dimensional vector matrices are used for calculation. Part A) is plane y=16 of the external magnetic field calculated using the analytic solution to the problem depicted in Figure 3.12. The surface vectors from this field were selected to be used for input into the Fourier radial iteration algorithm. Part B) shows plane y=16 of these surface vectors. The surface of the sphere is not well-defined in the 32x32x32 matrix, so in some places a thin shell of vectors was kept to ensure a closed surface of measurements. Finally, part C) shows the extrapolation of the surface values. Comparing graph C) to A) indicates how Fourier projection was able to accurately regenerate the missing field values.

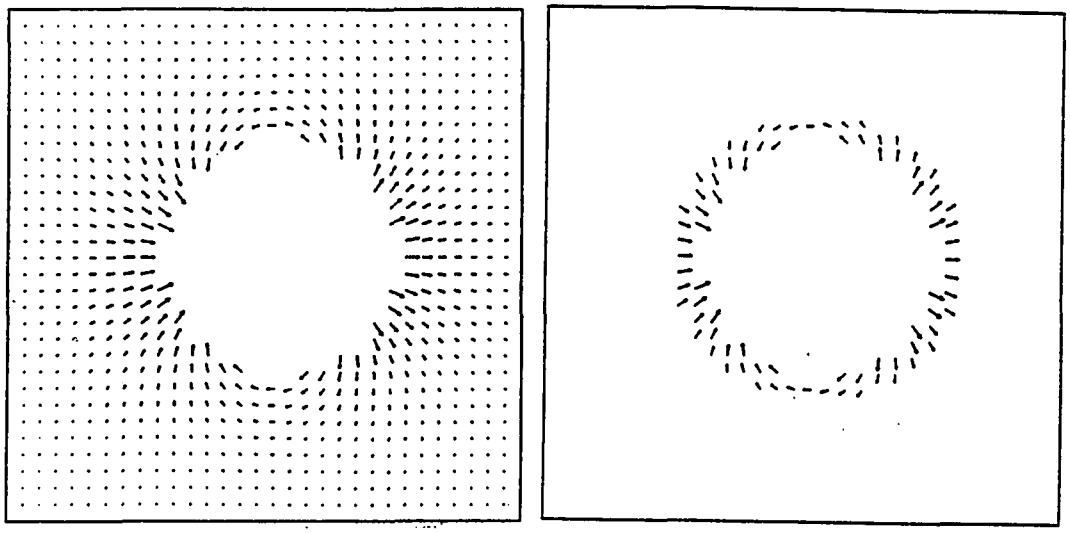

A

B

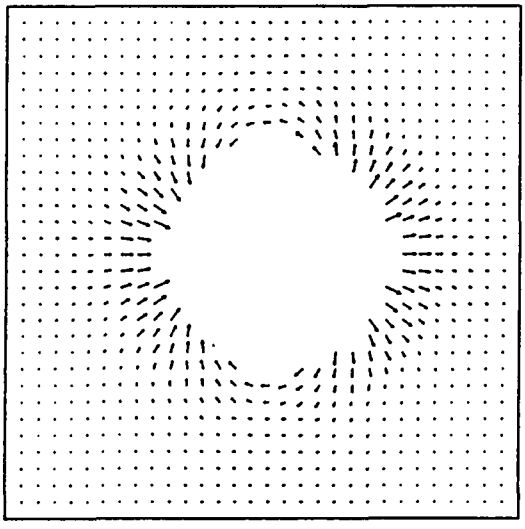

C

Figure 4.4: A) Analytic calculation of the magnetic field surrounding the sphere in Fig. 3.10 B) The surface values of field A C) Extrapolation of the surface values using Fourier projection. All three figures show plane y=16.

Internal Magnetic Field Reconstruction

The external magnetic field has now been generated, and the remaining problem is to calculate the internal field. In its present state, the external magnetic field is not a valid solution for the entire magnetic field because diverges into the internal region and thus has Fourier radial components. The Laplace equation is no longer viable means for filling the interior region because electric currents exist there. Strictly speaking, only two criteria determine the possible solutions at this point; the magnetic field must not have any divergence and must equal the values either measured or calculated in the external region.

A reasonable basis for reconstruction begins by removing the radial components with a Fourier tangential iteration. The Fourier tangential operation is applied until it no longer alters the external field from its known values. Three to ten iterations will usually suffice. Note that this is possible only if the original measurements establish a zero net flux across the surface of the volume. Legitimate magnetic fields naturally satisfy this prerequisite which in fact, may serve as an indication of field measurement accuracy.

As one might expect, the Fourier tangential procedure produces the field that is generated by currents confined to flow only at the surface of the volume. To see this, realize that the internal field is constructed using external dipole sources which introduce no internal curl. Furthermore, the external field was created according to the Laplace equation, so no curl exists externally either. Therefore, the only neighborhood for curl (or current $\nabla \times \mathbf{B} = \mathbf{J}$) is along the interface between internal and external fields.

Figure 4.5 is view of Figure 4.3 now completed using tangential reconstruction. Notice that curl exists only along the outline of the cubical region. The external field is the same as that in Figure 4.3, but the large internal field values have reduced the visibility of the external field somewhat. As indicated in Figure 4.1, the correct answer should be a vertical dipole field centered at the current loop. Instead, the solution generated is a smeared version spread rather uniformly throughout the cubical region.

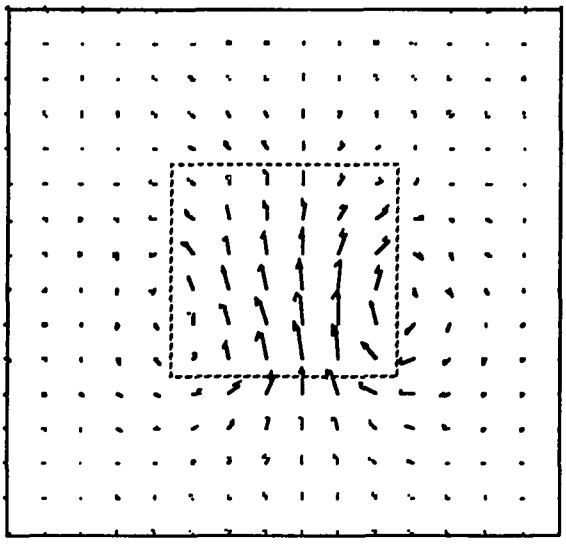

Figure 4.5: An internal solution for the magnetic field in Fig. 4.3.

Finally, Figure 4.6 presents a view of the currents which would have generated the magnetic field in Figure 4.5. This view is looking down upon the horizontal plane that contained the original current loop. Notice that the circulation of the current follows that of the original loop, but all of the current density has been transferred to the surface. Due to discretization, a divergenceless square loop is necessarily two pixels wide. The surface loops are repeated for each slice of the cube except the top and bottom surfaces which, as shown in Figure 4.7, have current spread more uniformly.

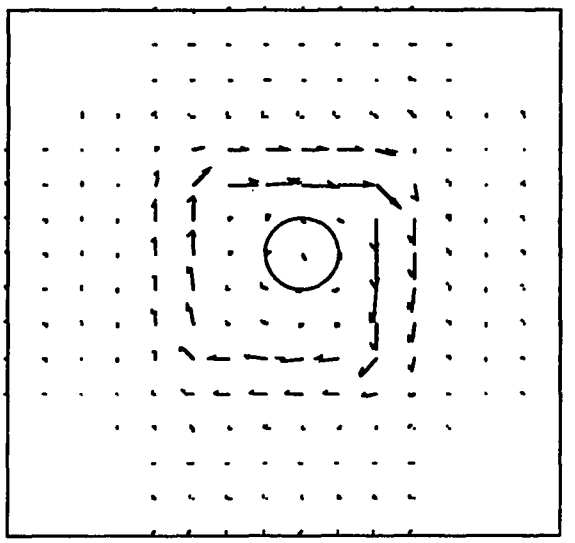

Figure 4.6: Plane z=6 of the current field that generates the magnetic field in Fig. 4.5. The circle represents the current that generated the original field in Fig. 4.2.

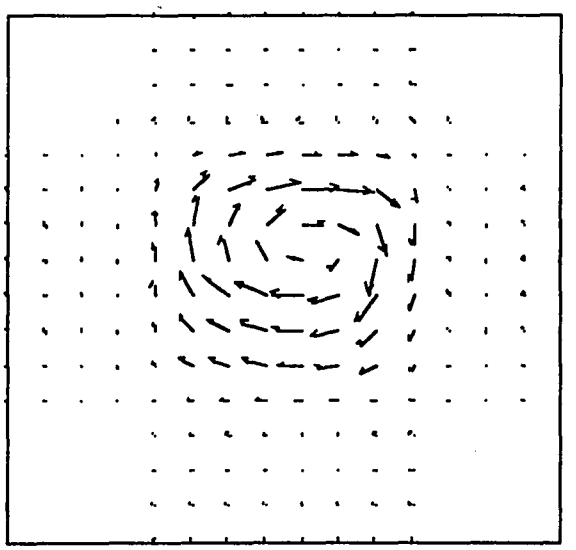

Figure 4.7: Plane z=10, the currents on the top surface of the cube.

Figure 4.8 shows the magnetic field resulting from a Fourier tangential iteration on the field in Figure 4.4 A). Again, the technique filled the interior rather uniformly and

generated curl only at the surface of the sphere. Figure 4.9 is plane x=16 of the corresponding surface currents. The correct answer should be a current dipole oriented in the z direction and located at (12,16,16).

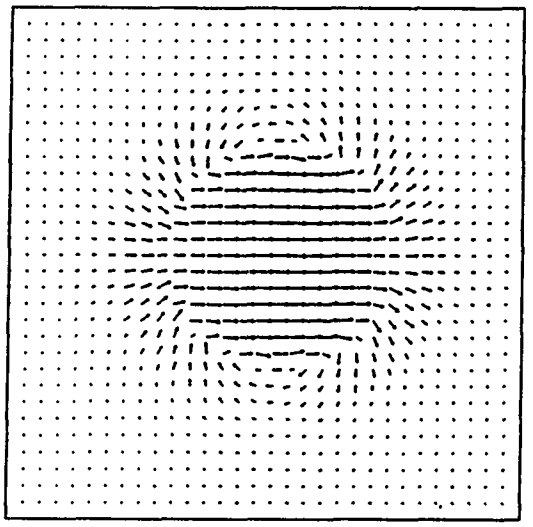

Figure 4.8: Plane y=16 of the magnetic field produced by a Fourier tangential iteration on the field in Fig. 4.4 A).

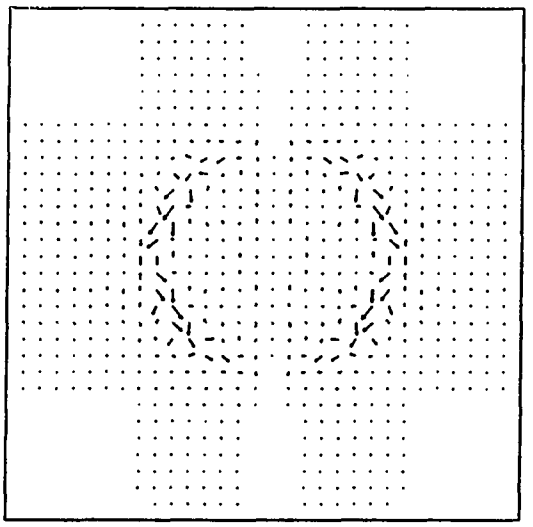

Figure 4.9: Plane x=16 of the surface currents that generated the field in Fig. 4.8.

The above results accentuate the nonuniqueness of the inverse problem. Fourier projection techniques reconstructed an internal magnetic field consistent with the external measurements yet different from the internal field known to exist. In terms of the inverse problem (from external magnetic field to internal current field), Fourier tangential iteration produces the equivalent surface current solution. Regardless of the actual internal current distribution, this Fourier technique will find the surface current distribution that generates the same external magnetic field.

The surface current solution is typically not the one desired, but it still contains useful information. For instance, if one has prior knowledge that the field in Figure 4.3 was generated by a current loop, the surface current solution may be used to localize the position of the actual loop. Figure 4.7 provides information for lateral location, and the depth position may be inferred by locating the z plane with the strongest surface currents. Thus, a directed search for specific current forms can extract functional information from surface current solutions. A goal for future research is to learn which current forms have diagnostic meaning and what constraints can be used to generate them.

Conclusion

This thesis has introduced a powerful new Fourier technique for solving boundary value problems. By decomposing mathematical fields into collections of electric and current dipole subfields, Fourier projection provides an interesting new perspective on vector calculus equations. The strengths of Fourier projection are its speed, stability, and ease of implementation. Its weakness comes from inaccuracies and artifacts introduced by discrete Fourier transforms. Because it concurrently operates in both real and reciprocal space, Fourier projection provides a unique environment in which to apply *a priori* constraints for ill-posed inverse problems. Frequency space filtering consistent with real space boundary conditions seems to be a promising means of reconstructing non-surface current solutions to the biomagnetic inverse problem. Lastly, Fourier projection techniques are not restricted to problems in biomagnetism and should prove useful for solving field equations encountered in a variety of disciplines.

Appendices

Appendix A

Here we derive the Fourier space equivalent of the Biot-Savart equation and in the process, show that

$$\text{F.T.}\left\{\frac{\mathbf{r}}{|r|^3}\right\} = \frac{-i2\rho}{\rho\cdot\rho}.$$

The Maxwell B-field equations and the Biot-Savart equation with their respective Fourier transforms are

$$\nabla\times\mathbf{B} = \frac{4\pi}{c}\mathbf{J} \quad\rightarrow\quad i2\pi\rho\times\tilde{\mathbf{B}} = \frac{4\pi}{c}\tilde{\mathbf{J}}$$

$$\nabla\cdot\mathbf{B} = 0 \quad\rightarrow\quad i2\pi\rho\cdot\tilde{\mathbf{B}} = 0$$

$$\mathbf{B} = \nabla\times\left(\mathbf{J}*\frac{1}{|r|}\right) \quad\rightarrow\quad \tilde{\mathbf{B}} = i2\pi\rho\times\tilde{\mathbf{J}}\,F.T.\left\{\frac{1}{|r|}\right\}.$$

Performing a ρ cross operation on the first expression and applying the BAC-CAB rule yields

$$\rho\times\left(i2\pi\,\rho\times\tilde{\mathbf{B}}\right) = i2\pi\rho\left(\rho\cdot\tilde{\mathbf{B}}\right) - \tilde{\mathbf{B}}\left(i2\pi\,\rho\cdot\rho\right)$$

$$\rho\times\frac{4\pi}{c}\tilde{\mathbf{J}} = -\tilde{\mathbf{B}}\left(i2\pi\,\rho\cdot\rho\right).$$

Thus, with c=1,

$$\tilde{\mathbf{B}} = \frac{i2\rho\times\tilde{\mathbf{J}}}{\rho\cdot\rho}.$$

When compared to the original Biot-Savart form, we find

$$F.T.\left\{\frac{1}{|r|}\right\} = \frac{1}{\pi(\rho\cdot\rho)}.$$

Or,

$$\boxed{F.T.\left\{\frac{\mathbf{r}}{|\mathbf{r}|^3}\right\}} = F.T.\left\{-\nabla\frac{1}{|\mathbf{r}|}\right\} = -i2\pi\rho\,\frac{1}{\pi(\rho\cdot\rho)} = \boxed{\frac{-i2\rho}{\rho\cdot\rho}}.$$

Appendix B

The external field calculation for a vertical dipole beneath an infinite plane:

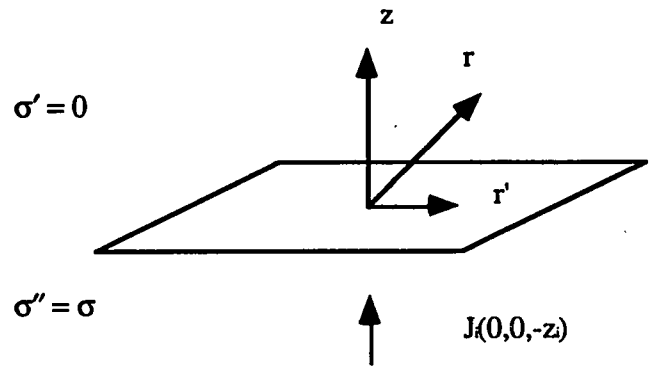

A vertical dipole impressed current source is placed a distance z_i beneath a plane interface at z=0. Beyond the plane, the conductivity is zero. Beneath, the conductivity is a constant value, σ. The current source is

$$\mathbf{J}_i(0,0,-z_i) = \begin{bmatrix} 0 \\ 0 \\ Q_z \end{bmatrix}\delta(x)\delta(y)\delta(z+z_i).$$

From Sarvas[1] equation (17), the magnetic field produced by impressed sources plus their return current is

$$\mathbf{B}(\mathbf{r}) = \mathbf{B}_0(\mathbf{r}) - \frac{\mu_0}{4\pi}\sum_{j=1}^{n}(\sigma_j' - \sigma_j'')\int_{S_j}\mathbf{V}(\mathbf{r}')\mathbf{n}(\mathbf{r}')\times\frac{\mathbf{r}-\mathbf{r}'}{|\mathbf{r}-\mathbf{r}'|^\beta}d\mathbf{S}_j.$$

For this example, $\mathbf{B}_0$ is the magnetic field produced by a current dipole in isotropic space

$$\mathbf{B}(\mathbf{r}) = \frac{\mu_0}{4\pi}\begin{bmatrix} Q_x \\ Q_y \\ Q_z \end{bmatrix} \times \frac{\mathbf{r}-\mathbf{r}'}{|\mathbf{r}-\mathbf{r}'|^3} = \frac{\mu_0}{4\pi|\mathbf{r}-\mathbf{r}'|^3}\begin{bmatrix} -Q_z y \\ Q_z x \\ 0 \end{bmatrix}.$$

Inserting this result yields

$$\mathbf{B}(\mathbf{r}) = \frac{\mu_0}{4\pi|\mathbf{r}-\mathbf{r}'|^3}\begin{bmatrix} -Q_z y \\ Q_z x \\ 0 \end{bmatrix} - \frac{\mu_0\sigma}{4\pi}\int_{-\infty}^{\infty}\int_{-\infty}^{\infty} \frac{V(x',y',0)}{|\mathbf{r}-\mathbf{r}'|^3}\begin{bmatrix} 0 \\ 0 \\ 1 \end{bmatrix} \times \begin{bmatrix} x-x' \\ y-y' \\ z \end{bmatrix} dx'dy'.$$

To solve this integral, we must know the electric potential on the surface, plane z=0. From Sarvas, equation (19), we have

$$\frac{\sigma_k'+\sigma_k''}{2}V(\mathbf{r}) = \sigma_n V_0(\mathbf{r}) - \sum_{j=1}^{n}\frac{\sigma_j'+\sigma_j''}{4\pi}\int_{S_j} V(\mathbf{r}')\mathbf{n}(\mathbf{r}')\cdot\frac{\mathbf{r}-\mathbf{r}'}{|\mathbf{r}-\mathbf{r}'|^3}dS_j.$$

And for a dipole current source, V_0 is

$$V(\mathbf{r}) = \frac{1}{4\pi\sigma|\mathbf{r}-\mathbf{r}_0|^3}\begin{bmatrix} Q_x \\ Q_y \\ Q_z \end{bmatrix} \cdot \begin{bmatrix} x \\ y \\ z+z_i \end{bmatrix}.$$

Using this result and integrating over the plane z=0 yields

$$\frac{\sigma}{2}V(\mathbf{r}) = \frac{1}{4\pi|\mathbf{r}-\mathbf{r}_0|^3}Q_x(z+z_i) - \frac{1}{(4\pi)^2}\int_{-\infty}^{\infty}\int_{-\infty}^{\infty} \frac{Q_z z_i}{|\mathbf{r}'-\mathbf{r}_0|^3|\mathbf{r}-\mathbf{r}'|^3}\begin{bmatrix} 0 \\ 0 \\ 1 \end{bmatrix} \cdot \begin{bmatrix} x-x' \\ y-y' \\ 0 \end{bmatrix} dx'dy'.$$

For all x' and y', the two vectors remain mutually orthogonal, so the integral equals zero, and the electric potential at the plane becomes

$$V(x,y,0) = \frac{Q_z z_i}{2\pi\sigma|\mathbf{r}-\mathbf{r}_0|^3}.$$

Thus, the potential at the plane is exactly twice what it would have been without the change in conductivity. This result confirms the intuitive solution found by placing an "image" dipole of equal magnitude but opposite orientation at position $z = +z_i$.

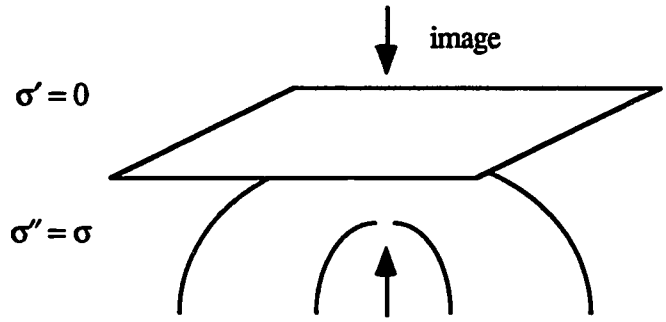

Knowing the voltage on the surface, we now may solve for the magnetic field everywhere

$$\mathbf{B}(\mathbf{r}) = \frac{\mu_0}{4\pi|\mathbf{r}-\mathbf{r}'|^3}\begin{bmatrix} -Q_z y \\ Q_z x \\ 0 \end{bmatrix} - \frac{\mu_0 Q_z \sigma}{8\pi^2}\int_{-\infty}^{\infty}\int_{-\infty}^{\infty} \frac{1}{|\mathbf{r}'-\mathbf{r}_0|^3|\mathbf{r}-\mathbf{r}'|^3}\begin{bmatrix} -(y-y') \\ x-x' \\ 0 \end{bmatrix} dx'dy'.$$

To verify that this is indeed equal to zero, we first examine the x component of the integral

$$q(x,y) = \int_{-\infty}^{\infty}\int_{-\infty}^{\infty} \frac{(y-y')}{\left[x'^2+y'^2+z_i^2\right]^{\frac{3}{2}}\left[(x-x')^2+(y-y')^2+z^2\right]^{\frac{3}{2}}} dx'dy'.$$

Notice that $q = \frac{\delta}{\delta y} p(x,y)$ where

$$p(x,y) = \int_{-\infty}^{\infty}\int_{-\infty}^{\infty} \frac{(y-y')}{\left[x'^2+y'^2+z_i^2\right]^{\frac{3}{2}}\left[(x-x')^2+(y-y')^2+z^2\right]^{\frac{1}{2}}} dx'dy'.$$

Let

$$f(x,y) = [x^2 + y^2 + z_i^2]^{-3/2} \quad \text{and} \quad g(x,y) = [x^2 + y^2 + z_i^2]^{-1/2}$$

such that p(x,y) may be expressed as the two dimensional convolution

$$p = f*g.$$

Since f and g are radially symmetric, the fourier transform of p may be expressed in terms of a bessel integral

$$\tilde{P}(\rho) = 2\pi \int_0^\infty rp(r)J_0(2\pi\rho r)\, dr.$$

From Gradshtein & Ryzhik[2] equations (6.554), we find

$$\tilde{F}(\rho) = 2\pi \int_0^\infty r(r^2+z_i^2)^{-\frac{3}{2}} J_0(2\pi\rho r)\, dr$$
$$= \frac{2\pi}{z_i} e^{-2\pi z_i \rho} \quad \text{(G.R. 6.554\#4)}$$
$$\tilde{G}(\rho) = 2\pi \int_0^\infty r(r^2+z^2)^{-\frac{1}{2}} J_0(2\pi\rho r)\, dr$$
$$= \frac{1}{\rho} e^{-2\pi z \rho} \quad \text{(G.R. 6.554\#1).}$$

By the convolution relation,

$$P(\rho) = F(\rho)G(\rho) = \frac{2\pi}{z_i}\left[\frac{1}{\rho} e^{-2\pi(z+z_i)\rho}\right],$$

which may be inverse transformed to find

$$p(r) = \frac{2\pi}{z_i}\left[r^2+(z+z_i)^2\right]^{-\frac{1}{2}} \quad \text{so that}$$
$$q(x,y) = \frac{\partial}{\partial y} p(x,y) = \frac{2\pi}{z_i}\left[r^2+(z+z_i)^2\right]^{-\frac{3}{2}}.$$

Therefore,

$$\frac{y}{\left[x^2+y^2+(z+z_i)^2\right]^{\frac{3}{2}}} = \frac{z_i}{2\pi}\int_{-\infty}^{\infty}\int_{-\infty}^{\infty} \frac{(y-y')}{\left[x'^2+y'^2+z_i^2\right]^{\frac{3}{2}}\left[(x-x')^2+(y-y')^2+z^2\right]^{\frac{3}{2}}}dx'dy'$$

and indeed, the x component of the magnetic field vanishes for all points above the plane z=0. By inspection, the y component similarly vanishes, and the total magnetic field above the plane is zero.

---

[1]Sarvas, J. Basic mathematical and electrical concepts of the biomagnetic inverse problem. Phys. Med. Biol., 1987 Vol. 32, No. 1, 11-22.

[2]Gradshtein, I.S. and I.M. Ryzhik Table of Integrals, Series, and Products. Academic Press, Inc. 1980.